JOURNAL OF GUIDANCE, CONTROL, AND DYNAMICS
Vol. 36, No. 2, March–April 2013

Autonomous Trajectory Planning for Rendezvous and Proximity Operations by Conic Optimization

Ping Lu* and Xinfu Liu†
Iowa State University, Ames, Iowa 50011

DOI: 10.2514/1.58436

Autonomous rendezvous and proximity operations of spacecraft require the capability of onboard planning and executing highly constrained trajectories without ground support. This paper presents a general and rigorous methodology and algorithmic procedure toward this goal with a target vehicle that can be in an arbitrary orbit. The rendezvous and proximity operations problem is formulated as a nonlinear optimal control problem, subject to various state and control inequality constraints and equality constraints on interior points and terminal conditions. By a lossless relaxation technique, a relaxed problem is formed, the solution of which is proven to be equivalent to that of the original rendezvous and proximity operations problem. The relaxed problem is then solved by a novel successive solution process, in which the solutions of a sequence of constrained subproblems with linear, time-varying dynamics are sought. After discretization, each of these problems becomes a second-order cone programming problem. Their solutions, if they exist, are guaranteed to be found by a primal-dual interior-point algorithm. The efficacy of the proposed methodology is strongly supported by numerical experiments.

I. Introduction

RENDEZVOUS and proximity operations (RPOs) refer to the maneuvers needed by a chaser spacecraft to arrive in the vicinity of a target spacecraft and accomplish the mission objectives such as flying around or docking with the target. The entire rendezvous mission consists of several phases, characterized by different trajectory requirements, navigation sensors used, operational considerations, and the nature of the maneuvers. A rendezvous mission is typically divided into far-field rendezvous, near-field rendezvous, and final approach. Goodman [1,2], Woffinden and Geller [3], and Goodman and Brazzel [4] provide comprehensive background on the history, technology development, and evolution on the subject. More recent technical activities in RPO design and analysis for the Orion Multi-Purpose Crew Vehicle can be found in [5,6].

This paper is focused on autonomous trajectory planning for the last phases of an RPO mission where the chaser is already relatively close to the target. By "autonomous" it is meant that the planning of the trajectory and generation of guidance commands are performed onboard without crew intervention or ground support (but with crew/ground monitoring whenever possible). Such technology would be imperative for time-critical missions and missions where ground support is unavailable or when communication delays cannot be ignored. Much of the current technology for near-field and proximity mission analysis and guidance is based on the Clohessy–Wiltshire (CW) equations [7]. Although the CW equations, a set of linear, time-invariant, differential equations, provide a convenient means to analyze and visualize the relative motion between the chaser and the target, thus allowing a variety of possible technical approaches for mission design and guidance, the basic underlying assumption of the target in a circular orbit is very restrictive [8]. A small eccentricity of the target orbit ($e < 0.1$) would already invalidate the CW equations for flight with modest duration. When the target is in a highly eccentric orbit, the relative motion can exhibit some surprising strongly time-dependent features that are very different from the solution of the CW equations [9]. Although linearized, time-varying equations for relative motion around a target in a noncircular orbit are available [10], the design of rendezvous maneuvers and control of final approach trajectory based on these equations are much more challenging and less intuitive. In addition, realistic final approach and docking involve a number of trajectory constraints for docking port alignment as well as safety and failure tolerance requirements. Without a reliable, efficient, and versatile algorithm, these complexities would render the problems of trajectory and guidance design a laborious trial-and-error endeavor. The objective of this paper is to develop a rigorous and systematic methodology that will allow all of the requirements of the problem to be formulated formally in the problem statement, and then the problem will be numerically solved reliably and autonomously.

Because RPO missions are usually subject to timing constraints by communication and illumination considerations, the RPO problem in an inverse-square gravity field is first formulated as a fixed-time fuel-optimal control problem. Trajectory constraints including those on terminal-condition, plume-impingement inhibition, approach corridor and hold points are all formulated as parts of the problem requirements. This highly constrained optimal control problem would pose a great challenge to most numerical methods, direct or indirect. For the problem to be solved onboard for autonomous trajectory planning and closed-loop guidance, reliability/robustness of the algorithm is of paramount importance. Inspired by the recent remarkable success of a second-order cone programming (SOCP)-based methodology in powered planetary landing guidance reported in [11–13] and a class of optimal control problems in [14], this work represents an effort to develop an SOCP-based method to solve the RPO problem. A standard SOCP problem is a convex optimization problem with a linear cost function, equality constraints, and second-order conic inequality constraints (linear inequality constraints are special cases of second-order cones) [15–17]. Modern primal-dual interior-point algorithms are perhaps the best way to find numerical solutions to SOCP problems [18–20]. Such an algorithm has polynomial complexity and upper bounds on operations and the number of iterations required to find the solution, all of which can be determined a priori, even though convergence is typically achieved much faster than those conservative bounds indicate; they guarantee convergence to the global optimal solution if the inequality constraints have an interior point. Employing a self-dual embedding technique allows the algorithm to start from a self-generated feasible point without the need for any user-supplied initial guesses, and the solution to the previous self-dual embedded problem will provide

Received 26 March 2012; revision received 13 July 2012; accepted for publication 14 July 2012; published online 7 February 2013.

*Professor, Department of Aerospace Engineering; plu@iastate.edu. Associate Fellow AIAA.

†Graduate Student, Department of Aerospace Engineering; xinfu@iastate.edu.

the solution to the original SOCP problem if the solution to the SOCP exists or the duality certificate to clearly inform the outcome if the SOCP problem has no solution. All of these traits offer the kind of advantages not matched by other direct or indirect approaches. The same features certainly make the proposed methodology appealing for potential onboard applications. Wang and Boyd [21] and Mattingley and Boyd [22] show some recent work in pushing for real-time applications of a certain class of convex optimization to which SOCP belongs.

Because an RPO mission takes much longer (thousands of seconds), the vehicle will travel a long distance during the mission. As a result, the constant-gravity simplification used in the powered landing problem [11–13] is no longer valid, and at the least the inverse-square nonlinear gravity model should be used. Of course, the intrinsic nonlinearity associated with a finite-thrust engine in the dynamic equations will still exist as in [11–13]. To apply an SOCP-based method, the dynamics have to be linear. To bridge this gap, a relaxation technique similar to that in [11–13] is used to formulate a relaxed optimal control problem related to the RPO problem. The relaxed problem has dynamics that are affine in the augmented control vector, and all the inequality constraints in the problem are second-order conic constraints. Considerable effort is devoted to rigorously establish that the solutions to the relaxed problem and the original RPO problem are equivalent. Thus, the relaxation causes no loss of feasibility or performance. To overcome the nonlinearity in the gravity model, another contribution of this paper is to develop and formalize an innovative solution framework in which the solution to the relaxed problem, hence the original problem, is successively approached by the solutions to a sequence of problems with "linear, time-varying" gravity. When the successive solution sequence converges, the solution to the original problem will have been obtained. After appropriate discretization, each of these problems becomes an SOCP problem, and the solution is reliably found by a primal-dual interior-point algorithm. In addition to the advantage of general applicability to RPO missions around a target on any Keplerian orbit (not necessarily circular), the proposed methodology is shown to allow convenient incorporation in the solution process of harmonics in the gravity field such as the J_2 terms as well as aerodynamic drag. The effects of these terms can be nonnegligible for high-precision trajectory planning of RPO missions in low Earth orbits. The effectiveness of the methodology is demonstrated by various missions for rendezvous and docking with targets on circular and highly eccentric orbits.

II. Problem Formulation

The dimensionless equations of motion of 3-D flight for a spacecraft in a Newtonian gravity field, expressed in an inertial coordinate frame, are given by

$$\dot{\boldsymbol{r}} = \boldsymbol{V}, \qquad \boldsymbol{r}(0) = \boldsymbol{r}_0 \tag{1}$$

$$\dot{\boldsymbol{V}} = -\frac{1}{\|\boldsymbol{r}\|^3}\boldsymbol{r} + \frac{\boldsymbol{T}}{m}, \qquad \boldsymbol{V}(0) = \boldsymbol{V}_0 \tag{2}$$

$$\dot{m} = -\frac{1}{\boldsymbol{v}_{\text{ex}}}\|\boldsymbol{T}\|, \qquad m(0) = m_0 \tag{3}$$

where the radius vector $\boldsymbol{r}$ is normalized by R_0, the radius of the Earth; the inertial velocity vector $\boldsymbol{V}$ is normalized by $\sqrt{g_0 R_0}$, with g_0 being the gravitational acceleration at R_0; the thrust acceleration vector $\boldsymbol{T}$ is the total thrust vector divided by $\tilde{m}_0 g_0$, where $\tilde{m}_0$ is a nominal mass (e.g., the initial mass of the vehicle); the dimensionless mass m is the current vehicle mass divided by $\tilde{m}_0$; and $\boldsymbol{v}_{\text{ex}} > 0$ is the dimensionless constant effective exhaust velocity of the engine(s). Finally, the differentiation in these equations is with respect to a dimensionless time that is real time normalized by $\sqrt{R_0/g_0}$. This non-dimensionalization is critical for the success of the optimization algorithm to be discussed later. The Euclidean norm for vectors is used throughout this paper. The initial conditions on $\boldsymbol{r}(0)$, $\boldsymbol{V}(0)$, and $m(0)$ are all given, unless otherwise stated.

Let $\boldsymbol{x} = (\boldsymbol{r}^T \boldsymbol{V}^T)^T$ be the trajectory state of the chaser, $\boldsymbol{x}_t(t) = (\boldsymbol{r}_t^T \boldsymbol{V}_t^T)^T$ be the state vector of the target, and t_f be the specified final time. Let the unit vector of the docking axis fixed with the target be represented by $1_n \in R^3$. See Fig. 1 for reference. Note that 1_n is moving with the target and thus a given function of time in the inertial frame. The performance index and constraints for the chaser spacecraft RPOs considered in this paper are

$$J = \int_0^{t_f} \|\boldsymbol{T}\| \, \mathrm{d}t \tag{4}$$

$$\boldsymbol{T} \le T_{\max} \tag{5}$$

$$\|\boldsymbol{r}(t) - \boldsymbol{r}_t(t)\| \cos\alpha \le {}^T_n(t)(\boldsymbol{r}(t) - \boldsymbol{r}_t(t)) \tag{6}$$

$${}^T_n(t)\boldsymbol{T} \le \|\boldsymbol{T}\| \cos\theta \tag{7}$$

$$C_f(t_f)\boldsymbol{x}(t_f) + \boldsymbol{d}_f(t_f) = 0 \tag{8}$$

$$C_i(t_i)\boldsymbol{x}(t_i) + \boldsymbol{d}_i(t_i) = 0, \quad i = 1, \ldots, l, \quad 0 < t_1 < \cdots < t_l < t_f \tag{9}$$

The performance index [Eq. (4)] is for minimum propellant consumption. The upper bound $T_{\max}$ (the maximum thrust magnitude divided by $\tilde{m}_0 g_0$) is engine dependent, and when $\|\boldsymbol{T}\| = 0$, the spacecraft is in a coast. Equation (6) specifies the rendezvous trajectory approach corridor defined by a cone with a half-angle of α deg at the docking bay of the target vehicle, as shown in Fig. 1, where α is usually $10 \sim 15$ deg. This constraint limits the final approach trajectory inside the conic corridor when the distance between the two vehicles is below a threshold value of typically 200 m.

The constraint in Eq. (7) represents one for thrust direction inhibition. The angle $\theta > 0$ is prescribed, representing the minimum angle by which the thrust plume of the chaser's engine must be pointed away from the target (the thrust plume direction is in the negative direction of $\boldsymbol{T}$) to avoid contamination to the target vehicle by the chaser's thruster plumes. This constraint, when necessary, is imposed only when the chaser is in close proximity of the target. Thus, the constraints of Eqs. (6) and (7) are not imposed until the chaser is in the proximity of the target.

The constraints in Eq. (8) specify the terminal conditions of the mission, for example,

$$\boldsymbol{x}(t_f) - \boldsymbol{x}_t(t_f) = 0 \tag{10}$$

for a rendezvous mission. In addition, at a prescribed sequence of times $t_i < t_f$, the chaser trajectory may be required to achieve certain conditions with respect to the target for operational considerations. For example, if the relative trajectory has a point on the same orbit as the target, it would provide an option for the chaser to maintain station keeping there without continuous propellant expenditure, should anything abnormal occur and the rendezvous maneuver needs to be temporarily halted. Such a trajectory protection requirement can be accommodated by the constraints of Eq. (9) with

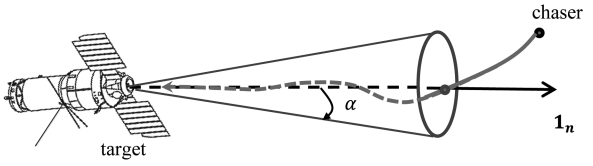

Fig. 1 Approach corridor for rendezvous defined by a cone with the docking axis n and apex half-angle α.

$$[\,I_{3\times3}\quad 0_{3\times3}\,]\qquad \boldsymbol{x}(t_i)-(\boldsymbol{r}_t(t_i)+\boldsymbol{\delta}_i)=0 \tag{11}$$

where $\boldsymbol{\delta}_i$ is a given position displacement vector from the target with desired direction and length. Appropriate choice of the $\boldsymbol{\delta}_i$ vector can specify a V-bar or an R-bar hold point, where the V-bar and R-bar directions are defined, respectively, by the local horizontal and the negative of radial directions of the target. The constraints of Eq. (9) may also be used to strategically place other way-points along the trajectory, such as an acquisition of docking axis (ADA) point constraint where the chaser relative trajectory is required to intersect with the docking axis. Note that the C_i and $\boldsymbol{d}_i$ at different interior points t_i need not have the same dimensions. This will allow the flexibility of constraining just the position, or both position and velocity at different points.

The RPO trajectory planning problem is to find the required thrust vector history $\boldsymbol{T}^*(t)$, such that, from the given initial condition $\boldsymbol{r}(0)$, $\boldsymbol{V}(0)$, and m_0, the chaser trajectory $\boldsymbol{x}(t)$ from the equations of motion [Eqs. (1)–(3)] and $\boldsymbol{T}^*(t)$ satisfy the constraints in Eqs. (5)–(9) while minimizing the performance index in Eq. (4). If this problem is repeatedly solved onboard with the current chaser state as the initial condition, the solution would provide closed-loop RPO guidance for the maneuver. It should be highlighted that the formulation of the RPO problem here, as well as the solution method to be seen later, does not rely on linearization or the assumption that the target is in a circular orbit. In fact, the target vehicle can be in any orbit, even with the effects of non-Newtonian gravity included. Section VI will provide more discussion in this regard.

III. Relaxation and Equivalence of Solutions

The dynamic equation [Eq. (3)] is nonlinear in the control $\boldsymbol{T}$, and the constraint of Eq. (7) is nonconvex if $0 \le \theta < \pi/2$. These two aspects must be "remedied", i.e., Eq. (3) rendered linear and Eq. (7) convexified in some way, if an SOCP approach is to be used to solve the problem numerically as in this paper. Toward this end, a slack control variable η is introduced in place of $\|\boldsymbol{T}\|$, and the original RPO problem in Eqs. (1)–(9) is relaxed to the following:

Given the dynamics

$$\dot{\boldsymbol{r}} = \boldsymbol{V}, \qquad \boldsymbol{r}(0) = \boldsymbol{r}_0 \tag{12}$$

$$\dot{\boldsymbol{V}} = -\frac{1}{\|\boldsymbol{r}\|^3}\boldsymbol{r} + \frac{\boldsymbol{T}}{m}, \qquad \boldsymbol{V}(0) = \boldsymbol{V}_0 \tag{13}$$

$$\dot{m} = -\frac{\eta}{\boldsymbol{v}_{\mathrm{ex}}}, \qquad m(0) = m_0 \tag{14}$$

minimize the performance index for a given $t_f > 0$:

$$J = \int_0^{t_f} \eta \,\mathrm{d}t \tag{15}$$

subject to

$$\|\boldsymbol{T}\| \le \eta \tag{16}$$

$$0 \le \eta \le T_{\max} \tag{17}$$

$$\|\boldsymbol{r}(t) - \boldsymbol{r}_t(t)\| \cos\alpha \le 1_n^T(t)[\boldsymbol{r}(t) - \boldsymbol{r}_t(t)] \tag{18}$$

$$1_n^T(t)\boldsymbol{T} \le \eta \cos\theta \tag{19}$$

$$C_f(t_f)\boldsymbol{x}(t_f) + \boldsymbol{d}_f(t_f) = 0 \tag{20}$$

$$C_i(t_i)\boldsymbol{x}(t_i) + \boldsymbol{d}_i(t_i) = 0, \quad i = 1,\ldots,l, \quad 0 < t_1 < \cdots < t_l < t_f \tag{21}$$

The previous problem is a relaxed version of the original problem, where the constraint in Eq. (5) is replaced by two relaxed ones in Eqs. (16) and (17), as is done in [11–13]. Now, the dynamics are linear in the augmented control vector $\boldsymbol{u} = (\boldsymbol{T}^T\eta)^T$, and the constraint in Eq. (19) becomes a linear inequality (thus a convex) constraint for any θ. See [13] for more discussion on this type of utilization. However, the solution to a relaxed problem in general may not be the solution, or even necessarily feasible, to the original problem. For the approach in this paper to be applicable, it is critical that the solutions to the relaxed and original problem are the same. Let us first make the following obvious observation.

Proposition 1: The original problem [Eqs. (1)–(9)] and the relaxed problem [Eqs. (12)–(21)] are equivalent if and only if the following condition holds in the solution to the relaxed problem almost everywhere (*a.e.*) in $[0, t_f]$:

$$\|\boldsymbol{T}\| = \eta \tag{22}$$

This equivalence is evident by comparing the two problems: the relaxed problem becomes the original problem if $\|\boldsymbol{T}\| = \eta$ almost everywhere in the solution of the relaxed problem. In fact, this condition is checked a posteriori in all of our numerical solutions to make sure that the solution found for the relaxed problem is indeed also that of the original problem. In the rest of this section, theoretical assurance of this equivalence is established.

Acikmese et al. [13] investigate the equivalence of the solutions of similarly posed problems for powered landing (earlier and less comprehensive versions of the problem and proofs can be found in [11,12]). The key differences between [13] and this paper are that, in [13], the gravity is constant (both in magnitude and direction), the constraints of Eq. (21) are not present, and an assumption is required that there are at most some isolated points on the trajectory where a state inequality constraint like Eq. (18) is active. In this paper, the gravity is from an inverse-square central force field; therefore, the system dynamics are nonlinear, and the multiple interior-point constraints impact the trajectory differently. More importantly, in our applications, frequently the optimal trajectory lies on the boundaries of inequality constraints for some finite durations. Hence, we will need to provide a general answer to the question of equivalence of solutions, including the case when the state inequality constraint of Eq. (18) is active in some subinterval(s) of finite length(s).

The following assumption will exclude a pathological case from consideration in the following theoretical investigation.

Assumption 1: If the constraint in Eq. (19) is present, the optimal trajectory of the relaxed problem [Eq. (12)–(21)] does not contain any finite segment where the pointing constraint [Eq. (19)] is active, while the following conditions hold simultaneously:

$$\frac{1_n^T(t)\boldsymbol{T}(t)}{\cos\theta} = \text{constant}, \quad \text{and} \quad 0 < \frac{1_n^T(t)\boldsymbol{T}(t)}{\cos\theta} < T_{\max} \tag{23}$$

Although it is probable that the constraint in Eq. (19) is active in a finite interval, the constancy condition in Eq. (23) is very restrictive, given that $1_n(t)$ and $\boldsymbol{T}(t)$ are both time-varying. The conditions in Eq. (23) render such optimal trajectory highly unlikely. If the constraint in Eq. (19) is not imposed, Assumption 1 is not needed.

First, a result is stated and proved for the case when the constraints of Eq. (21) are not considered.

Lemma 1: In the absence of the interior-point constraints [Eq. (21)] and under Assumption 1, if the optimal trajectory for the relaxed problem [Eqs. (12)–(20)] has no points where the constraint in Eq. (18) is active, the solution to the relaxed problem is identical to that of the original problem [Eqs. (1)–(8)] without the interior-point constraints of Eq. (9).

Proof: Suppose that $y^*(t) = (\boldsymbol{x}^{*T}(t)m^*(t))^T$ and $u^*(t) = (\boldsymbol{T}^{*T}(t)\eta^*)^T$ are the optimal state and control solutions to the problem [Eqs. (12)–(20)]. By the maximum principle [23], there exists in $[0, t_f]$ a continuous, nonzero costate vector function

$\boldsymbol{p}(t) = (\boldsymbol{p}_r^T(t)\boldsymbol{p}_V^T(t)p_m(t)p_0)^T$, where $\boldsymbol{p}_r \in R^3$, $\boldsymbol{p}_V \in R^3$, $p_m \in R$, and $p_0 \geq 0$ is a constant, such that, for the Hamiltonian H defined next,

$$H = \boldsymbol{p}_r^T\boldsymbol{V} + \boldsymbol{p}_V^T\left(-\frac{1}{\|\boldsymbol{r}\|^3}\boldsymbol{r} + \frac{\boldsymbol{T}}{m}\right) - \frac{p_m\eta}{\boldsymbol{v}_{\text{ex}}} - p_0\eta \tag{24}$$

the costates satisfy the following differential equations:

$$\dot{\boldsymbol{p}}_r = -\frac{\partial H}{\partial \boldsymbol{r}} = \frac{1}{\|\boldsymbol{r}\|^3}\boldsymbol{p}_V - \frac{3(\boldsymbol{p}_V^T\boldsymbol{r})}{\|\boldsymbol{r}\|^5}\boldsymbol{r} \tag{25}$$

$$\dot{\boldsymbol{p}}_V = -\frac{\partial H}{\partial \boldsymbol{V}} = -\boldsymbol{p}_r \tag{26}$$

$$\dot{p}_m = -\frac{\partial H}{\partial m} = \frac{(\boldsymbol{p}_V^T\boldsymbol{T})}{m^2} \tag{27}$$

Along the optimal trajectory for each fixed t, $\boldsymbol{y}^*(t)$, and the corresponding $\boldsymbol{p}(t)$, the optimal values $\boldsymbol{T}^*(t)$ and $\eta^*(t)$ are determined by pointwise maximization of H in Eq. (24) with respect to $\boldsymbol{T}$ and η [23]:

$$\max_{(T,\eta)\in\mathcal{U}} H[\boldsymbol{y}^*(t), \boldsymbol{p}(t), \boldsymbol{T}, \eta] \tag{28}$$

where

$$\mathcal{U} = \{(\boldsymbol{T}, \eta) | \|\boldsymbol{T}\| \leq \eta, 1_n^T(t)\boldsymbol{T} \leq \eta \cos\theta, 0 \leq \eta \leq T_{\max}\} \tag{29}$$

Furthermore, H is a constant along the optimal trajectory because the dynamics are autonomous, and this is a fixed-time problem. First, assume $\boldsymbol{p}_V \neq 0$ *a.e.* in $[0, t_f]$. Then, with respect to $\boldsymbol{T}$, H is a nonconstant, linear (thus convex) function. For each $\eta > 0$, the maximization of H with respect to $\boldsymbol{T}$ is performed over a bounded convex set:

$$\mathcal{U}_T = \{T | \|\boldsymbol{T}\| \leq \eta, 1_n^T(t)\boldsymbol{T} \leq \eta \cos\theta\} \tag{30}$$

A unique solution to this constrained pointwise maximization problem exists on the boundary of $\mathcal{U}_T$ [24], and it satisfies the Karush–Kuhn–Tucker (KKT) conditions [17] (for minimizing $f = -H$):

$$-\frac{\boldsymbol{p}_V}{m} + \frac{\lambda_1}{\|\boldsymbol{T}\|^2}\boldsymbol{T} + \lambda_2 1_n(t) = 0 \tag{31}$$

where

$$\begin{cases} \lambda_1 = 0 & \text{if } \|\boldsymbol{T}^*\| < \eta \\ \lambda_1 \geq 0 & \text{if } \|\boldsymbol{T}^*\| = \eta \end{cases}, \qquad \begin{cases} \lambda_2 = 0 & \text{if } 1_n^T(\text{t})\boldsymbol{T} < \eta\cos\theta \\ \lambda_2 \geq 0 & \text{if } 1_n^T(\text{t})\boldsymbol{T} = \eta\cos\theta \end{cases} \tag{32}$$

because the unique solution for the optimal $\boldsymbol{T}^*$ exists and must satisfy Eq. (31), which requires that $\lambda_1 \neq 0$. Thus, the constraint in Eq. (16) $\|\boldsymbol{T}\| \leq \eta$ must be active (i.e., $\|\boldsymbol{T}^*\| = \eta$). And it follows that $\|\boldsymbol{T}^*\| = \eta^*$ when η takes its optimal value. By Proposition 1, the solutions to the relaxed and original problems are the same.

Next, consider the case where $\boldsymbol{p}_V = 0$ in a finite interval in $[0, t_f]$. It follows from Eqs. (25) and (26) that we must have $\boldsymbol{p}_V = \boldsymbol{p}_r \equiv 0$ in $[0, t_f]$. Thus, $p_m =$ constant by Eq. (27). Because the final mass $m(t_f)$ is free, the transversality condition for $p_m(t_f)$ is [23]

$$p_m(t_f) = 0 \tag{33}$$

Therefore, $p_m \equiv 0$ in $[0, t_f]$. The Hamiltonian H in Eq. (24) in this case reduces to

$$H = -p_0\eta \tag{34}$$

Because $\boldsymbol{p}$ is nonzero, it must be true that the nonnegative p_0 is not zero (i.e., $p_0 > 0$), because already $\boldsymbol{p}_r = \boldsymbol{p}_V = p_m = 0$. The condition in Eq. (28) applied with respect to η means maximization of H in (34) over the set

$$\mathcal{U}_\eta = \{\eta | 1_n^T(t)\boldsymbol{T} \leq \eta\cos\theta, 0 \leq \eta \leq T_{\max}\} \tag{35}$$

The optimal η^* should then be the lower bound of the (nonempty) convex set $\mathcal{U}_\eta$. Given the required constancy of H, it is straightforward to verify that, under Assumption 1, the set $\mathcal{U}_\eta$ is equivalent to

$$\mathcal{U}_\eta = \{\eta | 0 \leq \eta \leq T_{\max}\} \tag{36}$$

Therefore, the lower bound of $\mathcal{U}_\eta$ is 0 and

$$\eta^* = 0 \tag{37}$$

As a consequence, constraint (16) admits only one solution $\boldsymbol{T}^* = 0$. But this again implies condition (22). It follows from Proposition 1 again that the solution to the relaxed problem is the same as that to the original problem.

When the inequality constraint in Eq. (18) becomes active in $[0, t_f]$ and/or when the interior-point constraints of Eq. (21) are added, what complicates the analysis is the fact that the costate will be only piecewise continuous, separated by the so-called jump conditions at the point(s) where the trajectory enters the boundary of constraint (18), and at the instances $t_1, \ldots, t_l$ where the constraints in Eq. (21) are imposed. Rewrite constraint (18) as

$$\|\boldsymbol{r}(t) - \boldsymbol{r}_t(t)\|\cos\alpha - 1_n^T(t)(\boldsymbol{r}(t) - \boldsymbol{r}_t(t)) := h(\boldsymbol{r}, t) \leq 0 \tag{38}$$

Constraint (38) is a second-order constraint with respect to the control vector $\boldsymbol{u}$, i.e., $\boldsymbol{T}$ (a part of $\boldsymbol{u}$) first appears in the second-order time derivative of $h(\boldsymbol{r}, t)$. Differentiating $h(\boldsymbol{r}, t)$ twice and using Eqs. (12) and (13) gives

$$\ddot{h} = \gamma^T(\boldsymbol{r}, t)\boldsymbol{T} + \varphi(\boldsymbol{r}, \boldsymbol{V}, t) := q(\boldsymbol{x}, \boldsymbol{T}, t) \tag{39}$$

Suppose that $[t_{\text{in}}, t_{\text{out}}] \subset [0, t_f]$ is an interval where constraint (38) becomes active. Then, the jump condition for the costates are [25]

$$\begin{pmatrix} \boldsymbol{p}_r(t_{\text{in}}^+) \\ \boldsymbol{p}_V(t_{\text{in}}^+) \end{pmatrix} = \begin{pmatrix} \boldsymbol{p}_r(t_{\text{in}}^-) \\ \boldsymbol{p}_V(t_{\text{in}}^-) \end{pmatrix} + \nu_1\frac{\partial h}{\partial \boldsymbol{x}} + \nu_2\frac{\partial \dot{h}}{\partial \boldsymbol{x}} \tag{40}$$

where ν_1 and ν_2 are two constant multipliers. Similarly, at the points $t_1, \ldots, t_l$, the interior-point constraints of Eq. (21) will cause jump conditions of the form [25]

$$\begin{pmatrix} \boldsymbol{p}_r(t_i^+) \\ \boldsymbol{p}_V(t_i^+) \end{pmatrix} = \begin{pmatrix} \boldsymbol{p}_r(t_i^-) \\ \boldsymbol{p}_V(t_i^-) \end{pmatrix} + C_i^T\nu_i, \qquad i = 1, \ldots, l \tag{41}$$

where ν_i is vector multiplier of appropriate dimension (the same as the row dimension of the C_i matrix). On the other hand, the following points should be made on the continuity of the Hamiltonian along the optimal trajectory of the relaxed problem:

1) Because the times $t_1, \ldots, t_l$ are specified, the Hamiltonian H is continuous across $t_1, \ldots, t_l$, despite the jumps in $\boldsymbol{p}_r$ and $\boldsymbol{p}_V$ at these points [25].

2) Likewise, it can be shown that the Hamiltonian is continuous at t_{in}, even though $\boldsymbol{p}_r$ and $\boldsymbol{p}_V$ are discontinuous in general at t_{in} due to Eq. (40). Parts of Theorems 5 and 22 in [23] on $H = 0$, with and without state inequality constraints, imply such continuity for free-time problems. A similar conclusion holds for the constancy of the Hamiltonian for fixed-time problems; thus, H remains continuous in $[0, t_f]$.

These jump conditions preclude the use of similar arguments as in the proof of Lemma 1 to establish the equivalence of the solutions and

necessitate a more involved approach. The following results will be used in this approach.

Lemma 2: If the solution to the relaxed problem [Eqs. (12)–(21)] contains any finite subinterval in $[0, t_f]$ where $\|\boldsymbol{T}^*\| < \eta^*$, i.e., the inequality in Eq. (16) holds strongly, this must be an interval where $\boldsymbol{p}_V = 0$.

The proof is given in Appendix A.

Lemma 3: Under Assumption 1, if the solution to the relaxed problem Eqs. (12)–(21) contains any finite subinterval of $[0, t_f]$ where $\boldsymbol{p}_V = 0$, the solution must have $\eta^* = T_{\max}$ in that interval.

The proof is provided in Appendix B.

Lemma 4: Under Assumption 1, the optimal solution to the relaxed problem Eqs. (12)–(21) satisfies the condition $\|\boldsymbol{T}^*\| = \eta^*$ *a.e.* in $[0, t_f]$

Proof: We shall prove the result by contradiction. Assume that there is a least one finite interval $[t_b, t_e] \subset [0, t_f]$, where $\|\boldsymbol{T}^*(t)\| = \beta(t) < \eta^*(t)$. By Lemma 2, this can only be an interval where $\boldsymbol{p}_V = 0$. By Lemma 3, this is also where $\eta^* = T_{\max}$. In the following, it will be shown that another feasible trajectory with a smaller cost can be constructed on the basis of these conditions to contradict the optimality of the given solution.

Because $\beta(t) < \eta^* = T_{\max}$ in $[t_b, t_e]$, it is always possible to find a function $\varepsilon(t)$ such that $\varepsilon(t_b) = 0$, $\varepsilon(t) > 0$, $\forall\ t \in (t_b, t_e]$, and

$$[1 + \varepsilon(t)]\beta(t) \le T_{\max} \tag{42}$$

Specifically, choose $\varepsilon(t)$ as

$$\varepsilon(t) = \frac{1}{2}\varepsilon_0(t - t_b)\left[1 + \frac{m^*(t_b)}{m^*(t)}\right], \qquad t \in [t_b, t_e] \tag{43}$$

where $m^*(t) = m^*(t_b) - T_{\max}(t - t_b)/v_{\text{ex}}$ is the optimal mass history in $[t_b, t_e]$ for the relaxed problem, and $\varepsilon_0 > 0$ a sufficiently small constant such that the condition of Eq. (42) remains true in the interval. Clearly such an ε_0 exists. For instance, let $\beta_{\max} = \sup \beta(t)$ for $t \in [t_b, t_e]$ (obviously, $\beta_{\max} < T_{\max}$ by the assumption that $\beta < T_{\max}$). Then, any ε_0 satisfying

$$0 < \varepsilon_0 \le (T_{\max}/\beta_{\max} - 1)/\{(t_e - t_b)[1 + m^*(t_b)/m^*(t_e)]\}$$

will do. Define a new thrust profile $\boldsymbol{T}$ in $[t_b, t_e]$ by

$$\boldsymbol{T}(t) = [1 + \varepsilon(t)]\boldsymbol{T}^*(t), \qquad t \in [t_b, t_e] \tag{44}$$

This $\boldsymbol{T}$ has the same direction as $\boldsymbol{T}^*$ but with greater magnitude, yet it is still admissible because of condition (42). Furthermore, define a function

$$\delta(t) = -\varepsilon_0 v_{\text{ex}} m^*(t) < 0, \qquad t \in [t_b, t_e] \tag{45}$$

Construct a control η in the interval

$$\eta(t) = T_{\max} + \delta(t) < T_{\max} = \eta^*, \qquad t \in [t_b, t_e] \tag{46}$$

The inequality holds because $\delta < 0$. Clearly, $\eta \ge 0$ when ε_0 is sufficiently small. Thus, this η is also admissible. Let

$$m(t) = m^*(t_b) + \int_{t_b}^{t} \dot{m}(\tau)\,\mathrm{d}\tau = m^*(t_b) - \int_{t_b}^{t} \frac{\eta(\tau)}{v_{\text{ex}}}\,\mathrm{d}\tau$$

be the mass profile from Eq. (14) corresponding to this η in the interval $[t_b, t_e]$ with the same initial condition $m(t_b) = m^*(t_b)$. It can be shown that

$$m(t) = [1 + \varepsilon(t)]m^*(t), \qquad t \in [t_b, t_e] \tag{47}$$

Note that there is no discontinuity in $m(t)$ at $t = t_b$ because $\varepsilon(t_b) = 0$. Hence, for this new admissible control $\boldsymbol{u} = (\boldsymbol{T}, \eta)$, the following equation holds:

$$\frac{\boldsymbol{T}(t)}{m(t)} = \frac{\boldsymbol{T}^*(t)}{m^*(t)}, \qquad t \in [t_b, t_e] \tag{48}$$

From Eqs. (12) and (13), condition (48) implies that, starting from the same condition as on the optimal trajectory at the beginning of the interval $[t_b, t_e]$, the trajectory for $\boldsymbol{x} = (\boldsymbol{r}^T \boldsymbol{V}^T)^T$ under the new control $\boldsymbol{u}$ in this interval will be identical to that of the optimal solution (therefore satisfying all trajectory constraints). In particular, at the end of the interval, $\boldsymbol{r}(t_e) = \boldsymbol{r}^*(t_e)$ and $\boldsymbol{V}(t_e) = \boldsymbol{V}^*(t_e)$, yet $m(t_e)$ now is greater than $m^*(t_e)$ because $|\dot{m}(t)| = \eta(t)/v_{\text{ex}} < T_{\max}/v_{\text{ex}} = |\dot{m}^*|$ in $[t_b, t_e]$. But this contradicts the fuel/mass optimality of the solution $\boldsymbol{y}^* = (\boldsymbol{r}^*(t), \boldsymbol{V}^*(t), m^*(t))$. Thus, the assumption that $\|\boldsymbol{T}^*\| < \eta^*$ in a finite interval cannot be true, and we must have $\|\boldsymbol{T}^*\| = \eta^*$ *a.e.* in $[0, t_f]$.

Note that Lemma 4 only states that $\boldsymbol{T}^* = \eta^*$ in the solution of the relaxed problem, but it does not suggest that $\eta^* = T_{\max}$ always. In fact, in a finite interval where constraint (18) is active where necessarily $\ddot{h} = \gamma^T(\boldsymbol{r}, t)\boldsymbol{T} + \varphi(\boldsymbol{r}, \boldsymbol{V}, t) = 0$ [cf. Eq. (39)], it can be seen that, in general, $\eta^* = \|\boldsymbol{T}^*\| < T_{\max}$ in a finite interval where $h \equiv 0$.

Combining Lemma 4 and Proposition 1, the following is concluded.

Proposition 2: Under Assumption 1, the solutions to the relaxed problem [Eqs. (12)–(21)] and the original problem in Eqs. (1)–(9) are the same.

IV. Method of Successive Approximation

To numerically solve the relaxed problem in Eqs. (12)–(21) as an SOCP problem, the equations of motion must also be linear in the state. The nonlinearity in m in Eq. (13) can be circumvented by making the thrust acceleration vector a part of the control:

$$\tau = \frac{\boldsymbol{T}}{m} \tag{49}$$

Next, make a change of variable $z = \ln m$ as first proposed in [11], and define $\sigma = \eta/m$. The state equations [Eqs. (12)–(14)] then become

$$\dot{\boldsymbol{r}} = \boldsymbol{V} \tag{50}$$

$$\dot{\boldsymbol{V}} = -\frac{1}{\|\boldsymbol{r}\|^3}\boldsymbol{r} + \tau \tag{51}$$

$$\dot{z} = -\frac{1}{v_{ex}}\sigma \tag{52}$$

Let $\boldsymbol{y} = (\boldsymbol{r}^T \boldsymbol{V}^T z)^T$ be the state vector of the previous system and $\boldsymbol{u} = (\tau^T \sigma)^T$ be the control vector. The previous state equations can be cast as

$$\begin{aligned}\dot{\boldsymbol{y}} &= \begin{bmatrix} 0_{3\times3} & I_{3\times3} & 0_{3\times1} \\ -\frac{1}{r^3}I_{3\times3} & 0_{3\times3} & 0_{3\times1} \\ 0_{1\times3} & 0_{1\times3} & 0 \end{bmatrix}\boldsymbol{y} + \begin{bmatrix} 0_{3\times3} & 0_{3\times1} \\ I_{3\times3} & 0_{3\times1} \\ 0_{1\times3} & -1/v_{\text{ex}} \end{bmatrix}\boldsymbol{u} \\ &=: A(r)\boldsymbol{y} + B\boldsymbol{u}\end{aligned} \tag{53}$$

where $r = \|\boldsymbol{r}\|$. The constraints in Eqs. (16) and (17) are now replaced by

$$0 \le \sigma \le T_{\max} e^{-z} \tag{54}$$

$$\|\tau\| \le \sigma \tag{55}$$

Using the variable σ, the performance index can also be changed to

$$J = \int_0^{t_f} \sigma\,\mathrm{d}t \tag{56}$$

It is readily seen that performance index (56) is equivalent to Eq. (15). An unintended consequence is that the right-hand side of the constraint in Eq. (54) is not a conic constraint anymore. To approximate it by a conic one, the term e^{-z} is expanded by a first-order Taylor series about a reference $z_0(t)$ [11,12]. More will be said about $z_0(t)$ later. Thus, the constraint in Eq. (54) is now represented by a linear constraint:

$$0 \le \sigma \le T_{\max} e^{-z_0(t)}[1 - (z(t) - z_0(t))] \tag{57}$$

It should be mentioned that constraint (54) includes constraint (57), i.e., any σ satisfying Eq. (57) also satisfies Eq. (54) [11]. Now, the only nonlinearity in the state equations is in the term $1/\boldsymbol{r}^3$ in the A matrix. In many cases, the percentage of variations for r is very small, and the approximation of $r \approx r_0$ may suffice, where r_0 is the initial radius. This is exactly the basis for the so-called "linear gravity" model proposed by Jezewski [26]. In such a case, A is a constant matrix, and the dynamics in Eq. (53) are linear. As a more general approach applicable to all cases with high precision, a successive solution method is devised in this paper. In this approach, the following procedure is taken to find the solution of the relaxed problem.

1) Set $k = 1$, and $r^{(0)}(t) = r_0$, and $z^{(0)}(t) = \ln(1 - \dot{m}_c t)$, where $\dot{m}_c > 0$ is an arbitrary constant dimensionless mass rate such that for the given final time t_f, $\dot{m}_c t_f \le m_p$ with m_p as the (dimensionless) propellant mass carried by the vehicle. A simple choice is

$$\dot{m}_c = \frac{m_p}{t_f} \tag{58}$$

2) Solve the following optimal control problem to find the solution pair $\{\boldsymbol{u}^{(k)}, \boldsymbol{y}^{(k)}\}$.

Given the state equations and initial condition:

$$\dot{\boldsymbol{y}}^{(k)} = A[r^{(k-1)}(t)]\boldsymbol{y}^{(k)} + B\boldsymbol{u}^{(k)}, \qquad \boldsymbol{y}^{(k)}(0) = \boldsymbol{y}(0) \tag{59}$$

minimize for the given t_f

$$J = \int_0^{t_f} \sigma^{(k)}(t)\,\mathrm{d}t \tag{60}$$

subject to

$$0 \le \sigma^{(k)}(t) \le T_{\max} e^{-z^{(k-1)}(t)}\{1 - [z^{(k)}(t) - z^{(k-1)}(t)]\} \tag{61}$$

$$\|\boldsymbol{\tau}^{(k)}(t)\| \le \sigma^{(k)}(t) \tag{62}$$

$$\|\boldsymbol{r}^{(k)}(t) - \boldsymbol{r}_t(t))\| \cos\,\alpha \le 1_n^T(t)[\boldsymbol{r}^{(k)}(t) - \boldsymbol{r}_t(t)] \tag{63}$$

$$1_n^T \boldsymbol{\tau}^{(k)}(t) \le \sigma^{(k)}(t) \cos\,\theta \tag{64}$$

$$C_f(t_f)\boldsymbol{x}^{(k)}(t_f) + \boldsymbol{d}_f(t_f) = 0 \tag{65}$$

$$C_i(t_i)\boldsymbol{x}^{(k)}(t_i) + \boldsymbol{d}_i(t_i) = 0, \quad i = 1, \ldots, l, \quad 0 < t_1 < \cdots < t_l < t_f \tag{66}$$

where $\boldsymbol{x}^{(k)} = \mathrm{col}(\boldsymbol{r}^{(k)}\boldsymbol{V}^{(k)})$, and $\boldsymbol{r}^{(k-1)}(t) = \|\boldsymbol{r}^{(k-1)}(t)\|$ and $z^{(k-1)}(t)$ are already found from the previous solution.

3) Check to see whether the convergence condition has been met for a prescribed tolerance $\varepsilon > 0$

$$\sup_{0 \le t \le t_f} \|\boldsymbol{y}^{(k)}(t) - \boldsymbol{y}^{(k-1)}(t)\| \le \varepsilon, \qquad k > 1 \tag{67}$$

If the previous condition is satisfied (for $k > 1$), go to step 4, otherwise, set $k = k + 1$, and go to step 2.

4) The solution to the problem is found to be $\boldsymbol{y} = \boldsymbol{y}^{(k)}$ and $\boldsymbol{u} = \boldsymbol{u}^{(k)}$. Stop.

The following remarks may be made.

a) For each k, the problem [Eqs. (59)–(66)] is one with linear, time-varying dynamics, linear equality constraints, and second-order-cone inequality constraints. Yet, it is still a nonlinear optimal control problem (because of the conic constraints) but is ready to be discretized into an SOCP problem and solved numerically.

b) The previous problems do not involve linearization in the conventional sense of small perturbations. The converged solution found is the one that satisfies exactly (to the accuracy of the numerical solution) the original nonlinear gravity model. On a related note, a successive solution approach is proposed in [27] to find the solution satisfying the linearized dynamics (in the conventional sense) in the proximity of a small celestial body, starting from a polynomial initial guessed trajectory.

3) The previous procedure suggests that, even if the linear gravity approximation is accurate (e.g., RPO trajectories near a circular orbit), at least two successive solutions will be needed in most cases because the optimal thrust profile (which consists of bang–bang structure in most cases) is unknown. Compared to [28], where the linear gravity model is used to solve for an optimal multiple-burn ascent trajectory all at once, the major difference is that the burn–coast structure (the number of burn and coast arcs) is specified in the problems treated in [28]. Here, no such information is prescribed a priori. Consequently the initial guessed mass profile defined by $z^{(0)}(t)$ is generally far from the final solution. However, the final solution found here will automatically determine the optimal number of burn and coast arcs as well as their durations in a problem.

Finally, a complete rendezvous mission is typically divided into several phases, (e.g., far-field phasing, near-field maneuvers, and final approach), each having distinctly different primary objectives and requirements, and relying on different navigation means and propulsion systems. It may be beneficial for the planning of an RPO trajectory to determine the best initial condition that will in turn serve as the target condition for the preceding phase. In such a case, the initial condition (position and velocity vectors) in Eq. (53) may be treated as unspecified and to be optimized subject to the box constraints:

$$\boldsymbol{r}_L \le \boldsymbol{r}^{(k)}(0) \le \boldsymbol{r}_U, \qquad \boldsymbol{V}_L \le \boldsymbol{V}^{(k)}(0) \le \boldsymbol{V}_U \tag{68}$$

where $\boldsymbol{r}_L$, $\boldsymbol{r}_U$, $\boldsymbol{V}_L$, and $\boldsymbol{V}_U$ are all in R^3 and prescribed.

V. Convergence of Successive Solutions

As the equivalence of the solutions of the relaxed problem and the original problem has already been established, our attention turns to the convergence of the solution sequence $\{\boldsymbol{y}^{(k)}\}$ in Sec. IV to the solution of the relaxed problem.

The closest resemblance in the literature to the approach in this paper is the work in [29]. The optimal control problem considered there is one with nonlinear system dynamics of the form

$$\dot{x} = A(\boldsymbol{x})\boldsymbol{x} + B(\boldsymbol{x})\boldsymbol{u}, \qquad \boldsymbol{x}(0) = \boldsymbol{x}_0 \tag{69}$$

with performance index

$$J = \frac{1}{2}\boldsymbol{x}^T(t_f)F\boldsymbol{x}(t_f) + \frac{1}{2}\int_0^{t_f}[\boldsymbol{x}^T Q(\boldsymbol{x})\boldsymbol{x} + \boldsymbol{u}^T R(\boldsymbol{x})\boldsymbol{u}]\,\mathrm{d}t \tag{70}$$

where $F \ge 0$, $Q(\boldsymbol{x}) \ge 0$, and $R(\boldsymbol{x}) > 0$ for all $\boldsymbol{x}$. The solution to the previous problem is found by solving successively the following time-varying linear quadratic regulator problems:

$$\dot{\boldsymbol{x}}^{(k)} = A(\boldsymbol{x}^{(k-1)})\boldsymbol{x}^{(k)} + B(\boldsymbol{x}^{(k-1)})\boldsymbol{u}^{(k)}, \qquad \boldsymbol{x}^{(k)}(0) = \boldsymbol{x}_0 \tag{71}$$

with quadratic performance index

$$J^{(k)} = \frac{1}{2}\boldsymbol{x}^{(k)T}(t_f)F\boldsymbol{x}^{(k)}(t_f) + \frac{1}{2}\int_0^{t_f}[\boldsymbol{x}^{(k)T}Q(\boldsymbol{x}^{(k-1)})\boldsymbol{x}^{(k)} + \boldsymbol{u}^{(k)T}R(\boldsymbol{x}^{(k-1)})\boldsymbol{u}^{(k)}]\,\mathrm{d}t \quad (72)$$

Assume that $A(\boldsymbol{x})$ satisfies the following conditions:

$$\mu(A(\boldsymbol{x})) \le \mu_0 \quad (73)$$

$$\|A(\boldsymbol{x}) - A(\boldsymbol{y})\| \le c\|\boldsymbol{x} - \boldsymbol{y}\| \quad (74)$$

for some positive constant μ_0 and c, where μ in Eq. (73) denotes the logarithmic norm of the matrix [30]. Under these two conditions and another pair of boundedness and Lipschitz conditions, the convergence of the previous solution sequence $\{\boldsymbol{x}^{(k)}\}$ is proved [29]. For time-invariant bilinear systems with quadratic performance index, Hofer and Tibken [31] and Aganovic and Gajic [32] also use an iterative approach that constructs a successive solution sequence, and the convergence of the solutions under a mild condition is proved.

For our problem, we first state an obvious fact based on the physics.

Proposition 3: Consider the system in Eqs. (1)–(3), subject to constraint (5). For a given $T_{\max}$ and fraction of propellant mass, there exist appropriate positive numbers $r_{\min}$, $r_{\max}$, $V_{\min}$, $V_{\max}$, $r_{0_{\min}}$, $r_{0_{\max}}$, $V_{0_{\min}}$, $V_{0_{\max}}$, $\gamma_{0_{\max}}$, and $t_{f_{\max}}$ such that, for any fixed $t_f \le t_{f_{\max}}$ and initial condition $(\boldsymbol{r}(0), \boldsymbol{V}(0)) \in X_0$ where

$$X_0 = \{(\boldsymbol{r}_0, \boldsymbol{V}_0) | r_{0_{\max}} \le \|\boldsymbol{r}_0\| \le r_{0_{\max}}, r_{0_{\min}} \le \|\boldsymbol{V}_0\| \le \boldsymbol{V}_{0_{\max}}, |\boldsymbol{r}_0^T\boldsymbol{V}_0| \le \|\boldsymbol{r}_0\|\|\boldsymbol{V}_0\|\sin(\gamma_{0_{\max}})\}$$

the trajectory will satisfy the following condition for any $\boldsymbol{T}(t)$ meeting $\|\boldsymbol{T}\| \le \boldsymbol{T}_{\max}$:

$$r_{\min} \le \|\boldsymbol{r}(t)\| \le r_{\max}, \quad \forall\ t \in [0, t_f] \quad (75)$$

$$V_{\min} \le \|\boldsymbol{V}(t)\| \le V_{\max}, \quad \forall\ t \in [0, t_f] \quad (76)$$

The previous conclusion can be easily proven, given that the unforced solution of the system is the well-understood Keplerian motion. For the relaxed problem with dynamics in Eqs. (12)–(14), subject to constraints (16) and (17), because $\|\boldsymbol{T}\| \le \eta \le T_{\max}$, the same conclusion will hold.

For our problem, the desired convergence of $\{\boldsymbol{y}^{(k)}\}$ to the solution of the original problem requires two prerequisites: 1) the relaxed problem [Eqs. (12)–(21)] has a solution, and 2) the original problem [Eqs. (1)–(9)] has a solution. Let $\mathcal{F}$ denote the set of feasible solutions to the relaxed problem [Eqs. (12)–(21)], i.e., $\mathcal{F}$ is the collection of all the solutions that satisfy Eqs. (12)–(14) and Eqs. (16)–(21). We have the following assurance regarding the existence of the solution(s).

Proposition 4: Assume that $\mathcal{F}$ is not empty, and the problem data are such that Proposition 3 holds. Then, the solution to the relaxed problem [Eqs. (12)–(21)] exists. Furthermore, if Assumption 1 in the preceding section is assumed to hold, the solution to the original problem [Eqs. (1)–(9)] also exists.

Proof: The proof of the existence of solution to the relaxed problem directly follows Corollary 2 in Chap. 4 of [33]. The relaxed problem is affine in the control $\boldsymbol{u} = (\boldsymbol{T}^T\eta)^T$, and so is the integrand in the performance index [Eq. (15)]. Proposition 3 ensures that the state trajectory of the problem is bounded. All other conditions required in Corollary 2 of [33] are satisfied. Corollary 2 does not include the interior-point constraints in Eq. (21) in the problem statement, but the addition of those will not change the proof and conclusion. Hence the solution to the relaxed problem exists. By Proposition 2 in the preceding section, the solution to the original problem is the same as that to the relaxed problem; hence, the solution to the original problem must exist as well.

As shown in [29] for quadratic problems, whether $\{\boldsymbol{y}^{(k)}\}$ converges heavily depends on the properties of the $A(r)$ matrix in Eq. (53). It can be shown that the $A(r)$ satisfies the following conditions:

$$\|A(r)\| = \frac{1}{r^3} \quad (77)$$

$$\|A(r_1) - A(r_2)\| = \left|\frac{1}{r_1^3} - \frac{1}{r_2^3}\right| \quad (78)$$

$$\mu(A(r)) = \frac{1}{2}\left(1 - \frac{1}{r^3}\right) \quad (79)$$

where the matrix norm is the spectral norm (maximum singular value). Because of the condition of Eq. (75), $\partial\|A(r)\|/\partial\boldsymbol{r} = -(3/r^5)\boldsymbol{r}$ and $\|-(3/r^5)\boldsymbol{r}\| \le 3\sqrt{3}/r_{\min}^4 := L$ in the closed bounded region of Eq. (75), we have

$$\|A(r_1) - A(r_2)\| \le L\|\boldsymbol{r}_1 - \boldsymbol{r}_2\| \quad (80)$$

$$\mu(A(r)) \le \frac{1}{2}\left(1 - \frac{1}{r_{\min}^3}\right) \quad (81)$$

Thus, the two most important conditions in [29] are met in our problem. But a complete theoretical proof of convergence of the successive solution sequence $\{\boldsymbol{y}^{(k)}\}$ appears much more difficult than in those cases reported in the literature because it is not a quadratic problem and, more fundamentally, there are various constraints [Eqs. (5)–(9)]. In a way, Proposition 4 also reveals why such a proof would be difficult; a proof the convergence of $\{\boldsymbol{y}^{(k)}\}$ would be equivalent to the proof of the existence of the solution to the original nonlinear optimal control problem in Eqs. (1)–(9). A general proof of the latter is likely to be rather elusive. However, given the naturally weak nonlinearity in the A matrix due to relatively small percentage of variations in r (recall the successful applications of linear gravity approximations [26,28]), it is rather natural in practice to expect convergence in just a few iterations. Our numerical experiences have always shown good convergence of the successive solutions, even in the case of highly eccentric orbits where the variations of r are not small.

Figures 2–4 illustrate the successive solution approach applied to an optimal ascent problem of a rocket. An ascent problem is chosen here for the demonstration because it has a much more appreciable difference between the first and the rest of the successive solutions than in a typical RPO problem. In this example, the initial condition corresponds to that of a typical launch ascent at the end of the endo-atmospheric ascent from the Kennedy Space Center to an orbit with

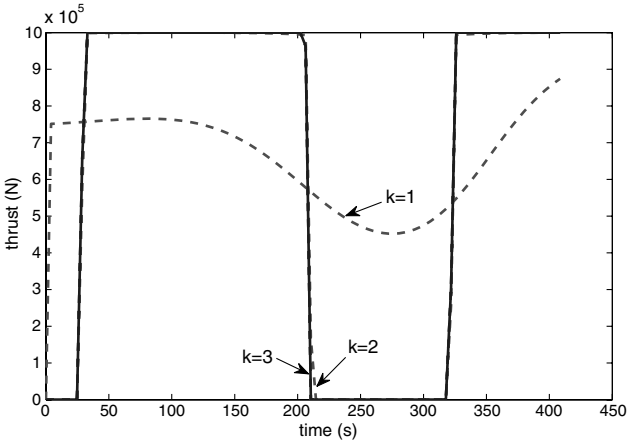

Fig. 2 Successive thrust profiles for the optimal upper-stage rocket ascent problem. Convergence is achieved in three iterations where k in the figure indicates the sequence of the successive solutions.

51.6 deg inclination. The final position and velocity are specified, specifying an elliptic orbit with eccentricity of 0.1 and semimajor axis of 7364.594 m. The upper stage is assumed to be able to fire multiple times, but the optimal number of burns is not known a priori. This would be a problem defined by Eqs. (1)–(5) and (8). Each of the relaxed problems as formulated in Sec. IV is discretized and solved as an SOCP problem, as described in Sec. VII. Figure 2 shows the thrust profiles of the successive solutions. For $k = 1$, the first solution is still very far from optimal because no knowledge of the optimal burn structure is available. But in three iterations, the solution converges to an optimal solution that consists of two pairs of coast–burn arcs. Figures 3 and 4 give the corresponding successive profiles in mass, altitude, and velocity. The convergence behavior seen in these figures is representative of what this approach routinely produces.

VI. Drag, J_2 Harmonic, and Docking Axis Uncertainty

Although the dynamic model in Eq. (2) only contains the inverse-square gravity acceleration, the effects of other terms not modeled in Eq. (2) may need to be incorporated in the RPO trajectory planning, depending on the altitude of the orbit. Among these terms, the most influential ones are perhaps the gravity due to the J_2 harmonic and aerodynamic drag. A major advantage of the approach in this paper, compared to using linearized dynamics as in [10], is that these terms can be included in the solution process without fundamental difficulty. For instance, the aerodynamic drag deceleration vector (in g) acting on the chaser can be represented by

$$\mathbf{D} = -\frac{1}{2\tilde{m}_0 g_0} R_0 \rho(r) V \qquad S_{\text{ref}} C_D \boldsymbol{V} := a_D(r, V)\boldsymbol{V} \tag{82}$$

where r and V are dimensionless as before, S_{ref} is the dimensional reference area of the chaser, ρ is the dimensional atmospheric density (which is altitude dependent), and C_D is the drag coefficient. Similarly, define the velocity component perpendicular to the $\boldsymbol{r}$ vector:

$$\boldsymbol{V}_h = \boldsymbol{V} - (\boldsymbol{V}^T \boldsymbol{r}/r^2)\boldsymbol{r} \tag{83}$$

Then, the gravitational acceleration due to J_2 harmonic in the gravitational potential can be expressed as

$$\begin{aligned} \boldsymbol{g}_{J_2} &= b_1 \boldsymbol{r} + b_2 \boldsymbol{V}_h + b_3 \boldsymbol{r} \times \boldsymbol{V} \\ &= [b_1 - b_2(\boldsymbol{V}^T \boldsymbol{r}/r^2)]\boldsymbol{r} + b_2 \boldsymbol{V} + b_3 \boldsymbol{r} \times \boldsymbol{V} \end{aligned} \tag{84}$$

where the scalars b_i are functions of $\boldsymbol{r}$ and $\boldsymbol{V}$, and their expressions can be readily found by comparing the terms of Eq. (84) with the J_2-related gravitational acceleration components in the directions of $\boldsymbol{r}$, $\boldsymbol{V}_h$ and $\boldsymbol{r} \times \boldsymbol{V}$ in [34]. When $\mathbf{D}$ and $\boldsymbol{g}_{J_2}$ are included, Eq. (2) will be modified to be

$$\dot{\boldsymbol{V}} = -\frac{1}{\|\boldsymbol{r}\|^3}\boldsymbol{r} + \mathbf{D} + \boldsymbol{g}_{J2} + \frac{\boldsymbol{T}}{m}, \qquad \boldsymbol{V}(0) = \boldsymbol{V}_0 \tag{85}$$

With $\mathbf{D}$ and $\boldsymbol{g}_{J_2}$ replaced by Eqs. (82) and (84), state equations (50, 85, 52) can be written as follows [as opposed to Eq. (53)]:

$$\dot{\boldsymbol{y}} = \tilde{A}(\boldsymbol{r}, \boldsymbol{V})\boldsymbol{y} + B\boldsymbol{u} + \zeta(\boldsymbol{r}, \boldsymbol{V}) \tag{86}$$

where the matrix $\tilde{A}$ has additional entries dependent on $\boldsymbol{r}$ and $\boldsymbol{V}$, as compared to A in Eq. (53), and

$$\zeta(\boldsymbol{r}, \boldsymbol{V}) = (0 \quad 0 \quad 0 \quad b_3(\boldsymbol{r} \times \boldsymbol{V})^T \quad 0)^T \tag{87}$$

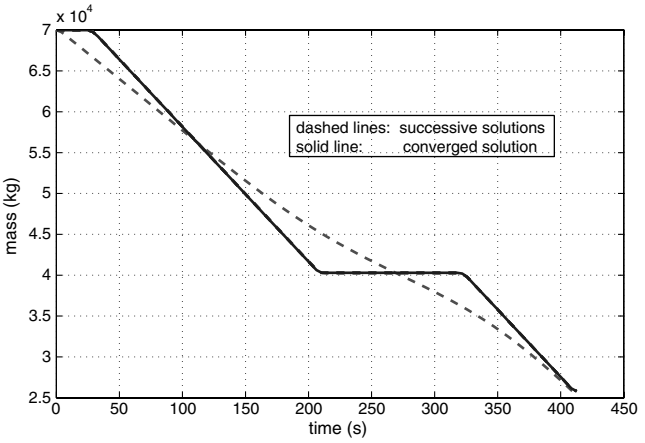

Fig. 3 Successive mass profiles for the optimal upper-stage rocket ascent problem. Note that the profile for $k = 2$ is indiscernible from the converged solution ($k = 3$) in the scale of the figure.

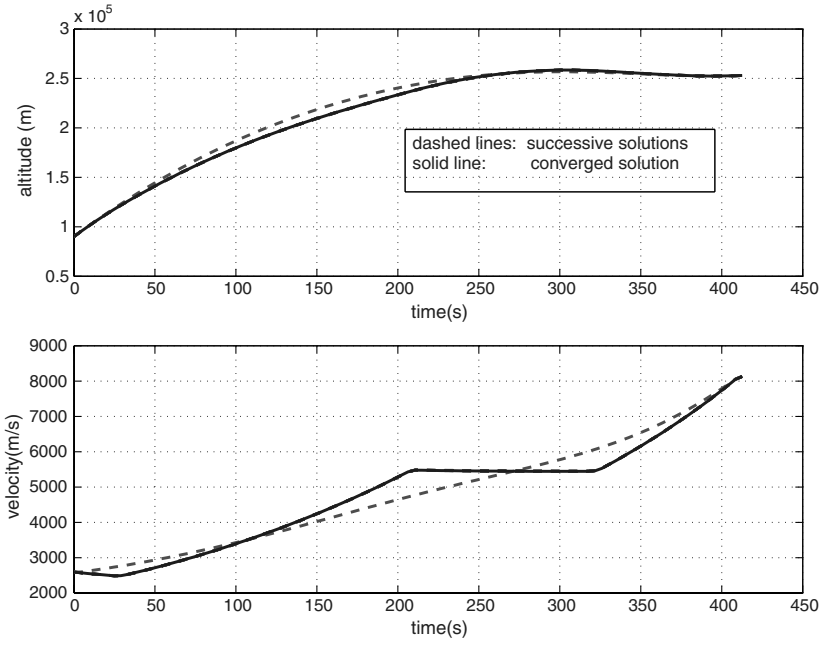

Fig. 4 Successive altitude and velocity profiles for the optimal upper-stage rocket ascent problem. Note that the profiles for $k = 2$ are indiscernible from the converged solution ($k = 3$) in the scale of the figure.

Then, in step 1 of the successive solution process of Sec. IV, set $\boldsymbol{r}^{(0)}(t) = \boldsymbol{r}_t(t)$ and $\boldsymbol{V}^{(0)}(t) = \boldsymbol{V}_t(t)$, and replace Eq. (59) in step 2 with

$$\dot{\boldsymbol{y}}^{(k)} = \tilde{A}_{k-1}(t)\boldsymbol{y}^{(k)} + B\boldsymbol{u}^{(k)} + \zeta_{k-1}(t), \qquad \boldsymbol{y}^{(k)}(0) = \boldsymbol{y}(0) \tag{88}$$

where $\tilde{A}_{k-1}(t) = \tilde{A}[\boldsymbol{r}^{(k-1)}(t), \boldsymbol{V}^{(k-1)}(t)]$ and $\zeta_{k-1} = \zeta[\boldsymbol{r}^{(k-1)}(t), \boldsymbol{V}^{(k-1)}(t)]$ are known in the kth successive solution. The rest proceeds as before. The discretized version of each problem for a fixed k is still an SOCP problem. The converged solution will have included the effects of the aerodynamic drag and J_2 harmonic in the gravitational acceleration. For a discussion of convergence of the successive solution sequence in which a free-drift term dependent on the previous solution, such as the term $\zeta_{k-1}(t)$ in Eq. (88) appears in the system equations, the reader is referred to [35].

Additional inequality state or control constraints can also be imposed on the trajectory, provided they are second-order cone, linear, or convex quadratic constraints. For example, the magnitude of the relative velocity may be constrained:

$$\|\boldsymbol{V}(t) - \boldsymbol{V}_t(t)\| \le \delta_V(t) \tag{89}$$

where $\delta_V > 0$ is prescribed and can be time-dependent. If needed, the previous constraint may be imposed at certain points (as additional interior-point inequality constraints) or over an interval of time (e.g., the last phase immediately before docking to increase the safety margin). The numerical-solution approach described in this paper will have no difficulty to incorporate such constraints. Furthermore, any convex, quadratic constraint of the form

$$x^T(t)P(t)\boldsymbol{x}(t) + 2\boldsymbol{q}^T(t)\boldsymbol{x}(t) + s(t) \le 0 \tag{90}$$

where $P > 0$, can be converted to a conic constraint [16] and hence enforced conveniently:

$$\|P^{1/2}\boldsymbol{x} + P^{-1/2}\boldsymbol{q}\| \le |\boldsymbol{q}^T P^{-1}\boldsymbol{q} - s|^{1/2} \tag{91}$$

Finally, the unit vector $1_n(t)$ representing the docking axis in constraint (6) has been assumed to be a deterministic vector thus far. Because of the small variations of the attitude of the target vehicle, $1_n(t)$ may be wobbling randomly about a mean direction at each point along the orbit of the target. Assume that, for each fixed t, $1_n(t)$ is a Gaussian random unit vector with a mean $\bar{1}_n(t)$ and covariance matrix $\Lambda(t)$. Suppose that we require the approach cone constraint [Eq. (6)] to be satisfied with a probability greater than or equal to a prescribed value of p where $0 < p \le 1.0$, that is,

$$\text{Prob}\{\|\boldsymbol{r}(t) - \boldsymbol{r}_t(t)\| \cos\alpha 1 \le_n^T (t)[\boldsymbol{r}(t) - \boldsymbol{r}_t(t)]\} \ge p \tag{92}$$

Following [16], it can be shown that the previous condition can be expressed as the following constraint:

$$\Phi^{-1}(p)\|\Lambda^{1/2}(\boldsymbol{r} - \boldsymbol{r}_t)\| + \cos\alpha\|\boldsymbol{r}(t) - \boldsymbol{r}_t(t)\|\bar{1} \le_n^T (\boldsymbol{r} - \boldsymbol{r}_t) \tag{93}$$

where Φ is the cumulative distribution function of a zero-mean, unit-variance Gaussian random variable:

$$\Phi(p) = \frac{1}{\sqrt{2\pi}}\int_{-\infty}^{p} e^{-\tau^2/2}\,\mathrm{d}\tau \tag{94}$$

and Φ^{-1} represents the quantile function. Assume $p \ge 0.5$. Then, $\Phi^{-1}(p) \ge 0$. Because

$$\begin{aligned}&\Phi^{-1}(p)\|\Lambda^{1/2}(\boldsymbol{r} - \boldsymbol{r}_t)\| + \cos\alpha\|\boldsymbol{r}(t) - \boldsymbol{r}_t(t)\| \\ &\quad \le \Phi^{-1}(p)\|\Lambda^{1/2}\|\|\boldsymbol{r} - \boldsymbol{r}_t\| + \cos\alpha\|\boldsymbol{r}(t) - \boldsymbol{r}_t(t)\| \\ &\quad = [\Phi^{-1}(p)\|\Lambda^{1/2}\| + \cos\alpha]\|\boldsymbol{r} - \boldsymbol{r}_t\|\end{aligned} \tag{95}$$

where again the matrix norm is spectral norm, enforcing the following second-order cone constraint will guarantee the satisfaction of the constraint in Eq. (93):

$$[\Phi^{-1}(p)\|\Lambda^{1/2}\| + \cos\alpha]\|\boldsymbol{r} - \boldsymbol{r}_t\| \le \bar{1}_n^T(\boldsymbol{r} - \boldsymbol{r}_t) \tag{96}$$

VII. Discretization

To find the numerical solution to the problem [Eqs. (59)–(66)] for each k, the state and control vectors are discretized by $\boldsymbol{y}_j = \boldsymbol{y}(t_j)$ and $\boldsymbol{u}_j = \boldsymbol{u}(t_j)$, $j = 1, \ldots, n$, where $t_j = jh$ and $h = t_f/n$ for an integer n. Note that some special attention may be needed if the interior-point constraints of Eq. (66) are required to be enforced exactly at the times t_i specified. A different discretization step size (smaller than h) can be taken just at the grid t_i so that t_i is exactly the one of the grid points for the discretization. The state equation (59) is integrated by trapezoidal rule:

$$\boldsymbol{y}_j = \boldsymbol{y}_{j-1} + \frac{1}{2}h[f(\boldsymbol{y}_j, \boldsymbol{u}_j, t_j) + \boldsymbol{f}(\boldsymbol{y}_{j-1}, \boldsymbol{u}_{j-1}, t_{j-1})], \qquad j = 1, \ldots, n \tag{97}$$

where $\boldsymbol{f}$ represents the right-hand side of Eq. (59), and $\boldsymbol{u} = (\boldsymbol{T}^T, \sigma)^T$. For each fixed k, let $A_j = A[r^{(k)}(t_j)]$. The previous equation leads to

$$\left(I - \frac{1}{2}hA_j\right)\boldsymbol{y}_j = \left(I + \frac{1}{2}hA_{j-1}\right)\boldsymbol{y}_{j-1} + \frac{1}{2}hB\boldsymbol{u}_j + \frac{1}{2}hB\boldsymbol{u}_{j-1} \tag{98}$$

where I is a 7×7 unit matrix. Note that this is a second-order integration scheme [36], equivalent to a local collocation scheme by a quadratic polynomial in each interval $[t_{j-1}, t_j]$. The local errors are proportional to h^3. At this point, two options may be considered in choosing the variables for the subsequent finite-dimensional optimization problem.

1) Choose the optimization vector to be $\boldsymbol{z} = (\boldsymbol{y}_0, \ldots, \boldsymbol{y}_n, \boldsymbol{u}_0, \ldots, \boldsymbol{u}_n)$. In this case, the collection of all the equations from Eq. (98) at each t_j forms linear equality constraints on $\boldsymbol{z}$. All of the constraints in Eqs. (61)–(66) will be enforced at t_j, effectively becoming linear equality and second-order conic inequality constraints on $\boldsymbol{z}$.

2) When $\boldsymbol{y}_0$ is given, all $\boldsymbol{y}_j$, $j = 1, \ldots, n$ can be recursively solved in terms of $\boldsymbol{u}_l$, $0 \le l \le j$, from Eq. (98):

$$\boldsymbol{y}_j = \left(I - \frac{1}{2}hA_j\right)^{-1}\left[\left(I + \frac{1}{2}hA_{j-1}\right)\boldsymbol{y}_{j-1} + \frac{1}{2}hB(\boldsymbol{u}_j + \boldsymbol{u}_{j-1})\right] \tag{99}$$

where the matrix inverse can be obtained explicitly as

$$\left(I - \frac{1}{2}hA_j\right)^{-1} = \begin{bmatrix} \frac{4r_j^3}{4r_j^3 + h^2}I_{3\times3} & \frac{2r_j^3 h}{4r_j^3 + h^2}I_{3\times3} & 0_{3\times1} \\ -\frac{2h}{4r_j^3 + h^2}I_{3\times3} & \frac{4r_j^3}{4r_j^3 + h^2}I_{3\times3} & 0_{3\times1} \\ 0_{1\times3} & 0_{1\times3} & 1 \end{bmatrix} \tag{100}$$

where $r_j = r^{(k)}(t_j)$. In this way, the $\boldsymbol{y}_j$ are replaced as linear functions of $\boldsymbol{u}_j$. The optimization variables are now just $\boldsymbol{z} = (\boldsymbol{u}_0, \ldots, \boldsymbol{u}_n)$. The discretized state equations [Eq. (98)] are no longer part of the optimization problem. The equality constraints and second-order cone constraints in Eqs. (61)–(66) will remain the same types of constraints for $(\boldsymbol{u}_0, \ldots, \boldsymbol{u}_n)$.

Discretization scheme 2 results in a significantly smaller dimension for the optimization problem when compared to scheme 1 (a 63.6% reduction, to be exact). But the problem under scheme 1 is sparse, whereas it is dense under scheme 2. The better choice of which scheme to use will depend on the optimization solver used (for instance, whether the software exploits sparsity in the problem for computation efficiency).

After the discretization, the problem [Eqs. (59)–(66)] now is reduced to an n_z-dimensional SOCP problem, where n_z is the dimension of the optimization variables after discretization, in the following form:

$$\min_{\boldsymbol{z}} \boldsymbol{c}^T\boldsymbol{z} \tag{101}$$

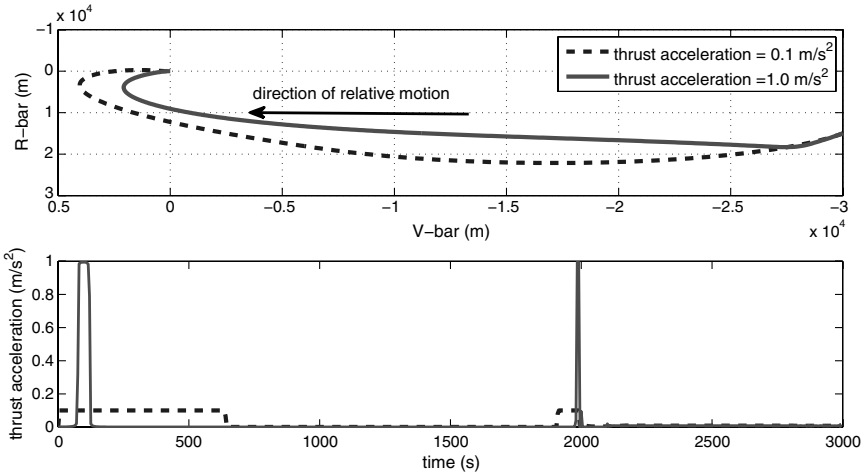

Fig. 5 Near-field rendezvous trajectories in the LVLH frame with a target (at the origin) in a 370 km circular orbit; two levels of maximum thrust acceleration used.

$$\|M_i z + \boldsymbol{b}_i\| \le \boldsymbol{e}_i^T z + f_i, \qquad i = 1, \ldots, N \tag{102}$$

where $M_i \in R^{n_i \times n_z}$, $n_i > 0$ is an integer, $\boldsymbol{c} \in R^{n_z}$, $\boldsymbol{b}_i \in R^{n_i}$, $\boldsymbol{e}_i \in R^{n_z}$, and f_i is a real number. Note that equality constraints are included in the constraints of Eq. (102) if, for some i, $M_i = M_{i+1} = 0$, $\boldsymbol{b}_i = \boldsymbol{b}_{i+1} = 0$, $\boldsymbol{e}_i = -\boldsymbol{e}_{i+1}$, and $f_i = -f_{i+1}$. A primal-dual interior-point algorithm can be used to solve the problem.

VIII. Numerical Demonstration

The methodology described in this paper has been implemented in YALMIP, a MATLAB-based rapid-algorithm development environment,[‡] and MOSEK, a primal-dual interior-point algorithm [20] for SOCP problems, for the following numerical results. No user-supplied initial guesses are needed by the algorithm. This means that all of the information about the solution, including trajectory, thrust profile (direction and magnitude), and optimal burn sequence (how many finite-time burns and when to start and end them), is all automatically determined by the algorithm. For each fixed k, the CPU time taken by MOSEK to solve each of the problems in Sec. IV on a typical desktop computer is a fraction of a second. The execution time is expected to be considerably shorter if a customized SOCP solver is developed that can take advantage of various techniques to speed up the computation (such as allowing warm start after the first solution has been found).

The spacecraft is assumed to have an initial mass of 1385 kg. Different levels of maximum thrust acceleration, ranging from 0.01 to 1.0 m/s^2 are used, depending on the mission scenarios examined. The coordinate system used to show the numerical results in the following is the standard local-vertical/local-horizontal (LVLH) frame, centered at the target vehicle. The local-horizontal axis (x axis) is also referred to as the V-bar axis, in the orbital plane of the target and pointing in the direction of orbital motion of the target. The local-vertical axis is positive down and is dubbed the R-bar axis.

A. Near-Field Rendezvous

For the near-field rendezvous missions shown, the vehicle's initial position is 30 km behind and 15 km below the target. Suppose that the docking axis is along the V-bar axis. The trajectory constraints for the mission are as follows.

Terminal constraints: At the specified final time $t_f = 3000$ s, the chaser's position and inertial velocity vectors match those of the target [cf. Eq. (8)].

ADA point constraints at $t = 2000$ s: The chaser trajectory intersects with the docking axis (the V-bar axis in this case) at $+200$ m from the target and has a velocity vector relative to the target pointing to the target long the negative V-bar axis with magnitude no greater than 0.1 m/s.

Approach cone constraint: Once within 200 m to the target, a 10 deg approach cone constraint [Eq. (6)] is enforced.

First, assume that the target is in a 370 km circular orbit. No knowledge about the optimal thrust profile, including the number of burns, thrust direction, and magnitude, is known a priori. The solution automatically determines all of it. Figure 5 shows, in the LVLH frame, the two rendezvous trajectories found, corresponding to maximum thrust accelerations of 0.1 and 1.0 m/s^2. It is seen that both optimal trajectories have two burns before entering the approach cone at $+200$ m on the V-bar axis: one at the initial part of the trajectories and the other right before the ADA point. Evidently, the usual "impulse" approximation is more appropriate for the case with thrust acceleration of 1.0 m/s^2 but not for the case with 0.1 m/s^2 thrust acceleration. It is interesting to note that, for higher thrust-acceleration, the first optimal burn did not take place until about 70 s from $t = 0$. Not discernible in the scale of the second plot in Fig. 5 are the thrust accelerations after 2000 s when the chaser enters the approach cone. The optimal thrust acceleration is much smaller (less than 0.01 m/s^2) inside the approach cone as the chaser moves along the boundary of the cone and needs to bring the relative velocity to zero when it arrives at the target (a similar phenomenon is plotted in Fig. 6).

It was pointed out earlier that the current methodology has no difficulty when the target is in a noncircular orbit, and no modifications of the algorithm are needed. To illustrate this point, the target is next assumed to be in an elliptic orbit with eccentricity of 0.5 and periapsis altitude of 370 km. At $t = 0$, it is assumed that the target is at the periapsis, and the chaser is still 30 km behind and 15 km below the target. The same constraints as used previously are imposed on the chaser trajectory. The optimal rendezvous trajectories corresponding to the two levels of thrust accelerations are plotted in Fig. 7. The arrowheads in the figure indicate the direction of the thrust vectors when the engine is on. Again, the optimal number of burns is found to be two up to the ADA point. It is observed that, for the first burn, the thrust vector is nearly perpendicular to the trajectory. The second burn, as seen from the second subplot of Fig. 7, is essentially a braking burn, where the thrust direction is nearly tangent to the trajectory but in the opposition direction of the relative motion. After the chaser enters the approach corridor, the engine burns continuously at intermediate value (similar to what will be seen in Fig. 6). It is interesting to note from the first plot of Fig. 7 that much of the chaser trajectory after the first burn corresponding to the higher thrust acceleration of 1.0 m/s^2 looks like a co-elliptic orbit used in space shuttle rendezvous [1]. But in actuality it is not a co-elliptic orbit, because at $e = 0.5$, the radial variations of the chaser in the LVLH frame would be at least several kilometers on a co-elliptic orbit, much more pronounced than what is seen in Fig. 7.

[‡]Data available online at http://users.isy.liu.se/johanl/yalmip/pmwiki.php?n=Main.HomePage [retrieved 29 January 2012].

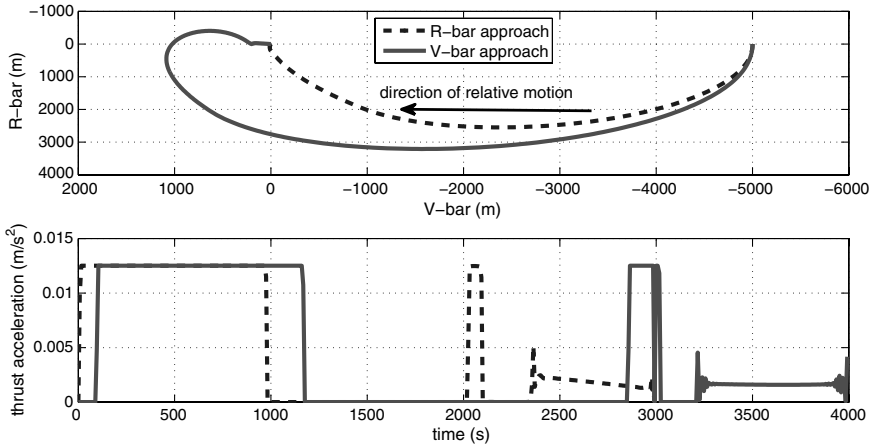

Fig. 6 Rendezvous trajectories to approach a target in a 370 × 13866 km elliptic orbit ($e = 0.5$) from R-bar and V-bar direction, respectively, with smaller thrusters than in Fig. 5.

B. Near-Field Rendezvous with Small Engines

At $t = 0$, the chaser is assumed to be on the same orbit as the target, but 5 km behind. Consider first the case again where the target is at the periapsis of an elliptic orbit with $e = 0.5$ and periapsis of 370 km. Smaller jets with maximum thrust acceleration at only 0.0125 m/s^2 are used for the maneuvers. Two cases are examined: 1) the chaser flies around and approaches the target along the (negative of) V-bar direction in 4000 s, and 2) an R-bar approach to the target in 3000 s. The same constraints on terminal conditions, ADA point, and approach cone as in the preceding subsection are imposed. Figure 6 shows the chaser trajectories in the LVLH frame and the thrust acceleration magnitudes in both cases. The second subplot of the figure illustrates the corresponding thrust acceleration profiles. Note that the optimal thrust is no longer bang–bang type during the last 200 m, where the trajectory is essentially moving along the boundary of the approach cone constraint in Eq. (6). Unlike in the soft landing applications in [11–13], here a state inequality constraint frequently becomes active in a time interval of nonzero length. This is an important reason why the theoretical investigation of the general equivalence of the solutions in Sec. III is needed.

Figure 8 compares V-bar fly-around and approach trajectories in the LVLH frame for a target in a 370 km circular orbit and a target in that elliptic orbit of $e = 0.5$. The top subplot also shows the thrust direction for the first long burn along each of the trajectories. The lower subplot zooms in on the last 200 m of the approach trajectories. The arrowheads again represent the direction of the thrust vector. The lower subplot of Fig. 8 clearly shows that the thrust direction is nearly along the radius direction; thus, plume impingement by the chaser thrust is not a concern. It can be seen that the relative trajectories in the LVLH frame do not differ significantly, despite the very different orbits of the target in the two cases. However, the inertial motion of the chaser is dramatically different in the two cases. The final altitude of the chaser is over 10,000 km when the target is in the elliptic orbit while the chaser altitude variations are less than 3 km when the target is in the circular orbit.

C. Approach and Docking

This phase of flight starts at the ADA point, 200 m from the target. The approach cone constraint in Eq. (6) is enforced throughout the entire trajectory. In addition, the relative velocity is constrained by

$$\|\boldsymbol{V} - \boldsymbol{V}_t\| \le \Delta V \tag{103}$$

where ΔV is set to be piecewise constant: $\Delta V = 0.2$ m/s when the distance to the target is greater than 100 m, $\Delta V = 0.1$ m/s when the distance is between 20 and 100 m, and $\Delta V = 0.03$ m/s when the distance to the target is within 20 m. The maximum acceleration of the chaser is limited to 0.01 m/s^2 in this phase.

Figure 9 shows the V-bar approach and docking trajectories and relative velocity variations for a target in a 370 km circular orbit. Three different mission durations of 2000, 2500, and 3000 s are used. Figure 10 gives the V-bar approach and docking trajectories and relative velocity variations for targets in three different elliptic orbits of $e = 0.3$, 0.5, and 0.7, all having a periapsis altitude of 370 km. At $t = 0$ the target is assumed to be at the periapsis. The mission times for all three cases are 2000 s. The trajectories in the LVLH frame are rather similar for these different values of eccentricity of the target's

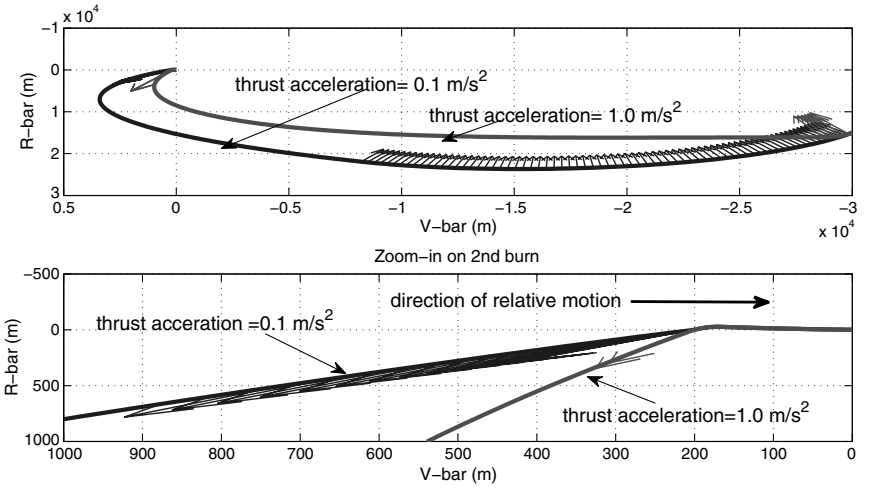

Fig. 7 Near-field rendezvous trajectories in the LVLH frame with a target in a 370 × 13866 km elliptic orbit ($e = 0.5$); the second subplot zooms in near the second burn.

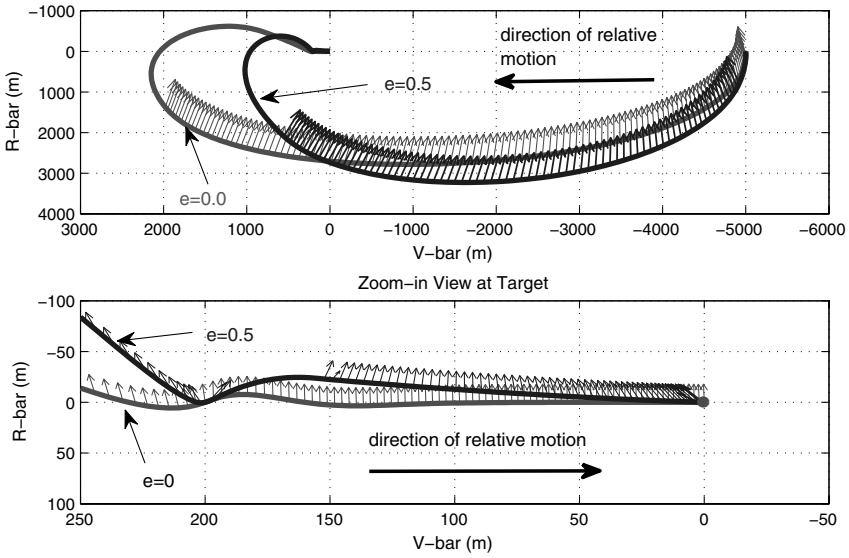

Fig. 8 Rendezvous trajectories in the LVLH frame for V-bar approach to a target in a 370 km circular orbit and 370 × 13866 km elliptic orbit ($e = 0.5$) with small thrusters.

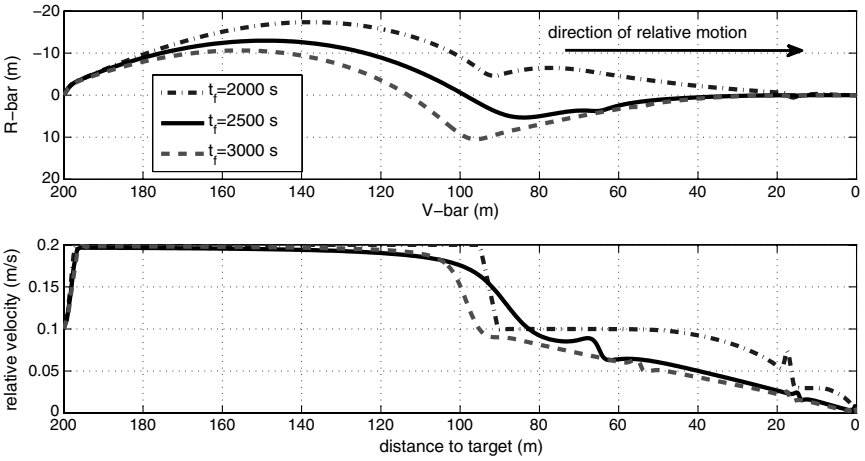

Fig. 9 V-bar approach and docking trajectories to a target in a 370 km circular orbit and corresponding relative velocity variations.

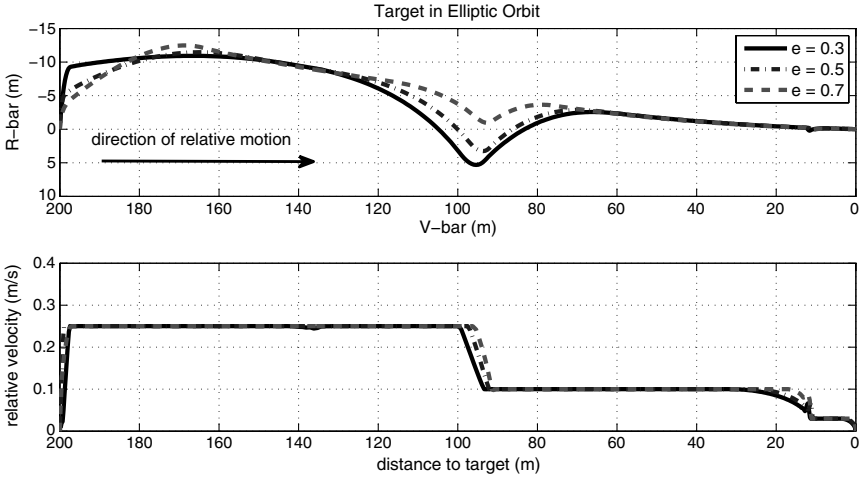

Fig. 10 V-bar approach and docking trajectories and corresponding relative velocity variations, for targets in 3 different elliptic orbits, all with periapsis altitude of 370 km and time duration of 2000 s.

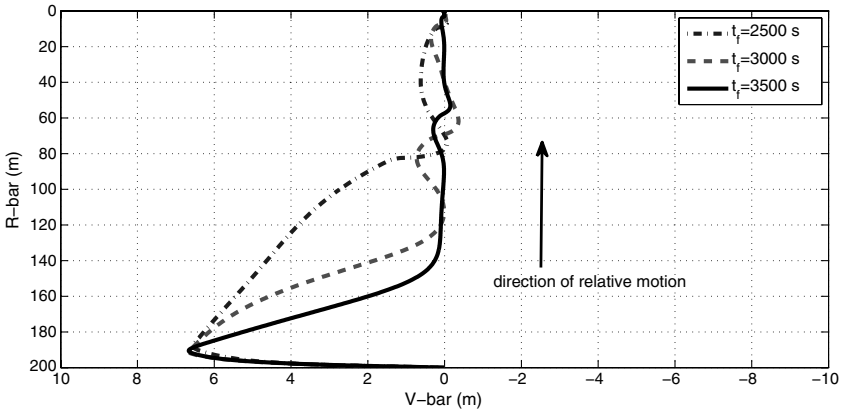

Fig. 11 R-bar approach and docking trajectories to a target in a 370 km circular orbit for three different values of mission duration.

orbit. And they are not drastically different from those in Fig. 9, where the target is in a circular orbit. The mission time of 2000 s does appear to be about the shortest possible, judging from the fact the relative velocity is on the boundary of the constraint Eq. (103) the entire time.

Finally, the R-bar approach and docking trajectories to a target in a 370 km circular orbit for three different mission durations are plotted in Fig. 11. Interestingly, the trajectory with the longest duration is the one that moves most closely along the R-bar axis most of the time.

IX. Conclusions

Autonomous trajectory planning for rendezvous and proximity operations (RPO) of spacecraft poses a great technical challenge because of the nonlinear trajectory dynamics, stringent constraints of various types, and high-precision requirement. This paper presents a new systematic and rigorous methodology for a reliable and rapid solution to the RPO problem, which is formulated as a nonlinear constrained optimal control problem. This development represents a major departure from the traditional approaches based on linearized dynamics of relative motion. The essential components of this methodology include lossless relaxation of the original RPO problem, a novel successive solution procedure, and utilization of a modern primal-dual interior-point algorithm for solutions of second-order cone programming problems, which is theoretically ensured (if solutions exist) in finite steps. The proposed method and algorithmic procedure are applicable to RPO missions where the target vehicle can be in any general orbit, require no externally supplied initial guesses, and enjoy high reliability of finding the solution. When necessary, J_2 terms in the gravity model and aerodynamic drag can be readily incorporated in the dynamic model by the proposed method. Clear evidence of effectiveness of the basic methodology has been demonstrated by numerical examples with the target vehicle in circular and highly eccentric orbits.

Appendix A: Proof of Lemma 2

We shall prove this lemma by showing that, if $\boldsymbol{p}_V \neq 0$ *a.e.*, then $\|\boldsymbol{T}^*\| = \eta^*$ must hold. First, assume that this interval where $\|\boldsymbol{T}^*\| < \eta^*$ does not overlap with the finite interval(s) where the constraint of Eq. (38) is active (if it happens at all). If $\boldsymbol{p}_V \neq 0$ *a.e.* in this interval, the pointwise maximization condition [Eq. (28)] applies. Following the same arguments based on the existence of a maximizing $\boldsymbol{T}^*$ and the KKT conditions as used in Lemma 1 shows, for any fixed $\eta \geq 0$,

$$\|\boldsymbol{T}^*\| = \eta \rightarrow \|\boldsymbol{T}^*\| = \eta^* \tag{A1}$$

that is $\|\boldsymbol{T}^*\| < \eta^*$ cannot be true in this interval.

Now, if the interval where $\boldsymbol{p}_V \neq 0$ *a.e.* overlaps with a finite interval where the constraint in Eq. (38) is active, the pointwise maximization condition [Eq. (28)] in this interval will be modified as (see the proof of Theorem 22 in [23] for detail[§]):

$$\max_{(T,\eta)\in\Omega(x)} H[\boldsymbol{y}(t), \boldsymbol{p}(t), \boldsymbol{T}, \eta] \tag{A2}$$

where H is the same as in Eq. (24), and the set $\Omega(\boldsymbol{x})$ is defined as follows: for given $\boldsymbol{x} = (\boldsymbol{r}^T \boldsymbol{V}^T)^T$, where $h(\boldsymbol{r}, t) = 0$,

$$\begin{aligned}\Omega(\boldsymbol{x}) = \{(\boldsymbol{T}, \eta) | \|\boldsymbol{T}\| \leq \eta, \gamma^T(\boldsymbol{r}, t)\boldsymbol{T} + \varphi(\boldsymbol{r}, \boldsymbol{V}, t) = 0,\\ 1_n^T \boldsymbol{T} \leq \eta \cos\theta, 0 \leq \eta \leq T_{\max}\}\end{aligned} \tag{A3}$$

where the second constraint $\gamma^T(\boldsymbol{r}, t)\boldsymbol{T} + \varphi(\boldsymbol{r}, \boldsymbol{V}, t) = 0$ is from Eq. (39). For each fixed $\eta > 0$, the domain from which $\boldsymbol{T}$ is selected to maximize H is the set $\omega(\boldsymbol{x})$:

$$\omega(\boldsymbol{x}) = \{\boldsymbol{T} | \|\boldsymbol{T}\| \leq \eta, \gamma^T(\boldsymbol{r}, t)\boldsymbol{T} + \varphi(\boldsymbol{r}, \boldsymbol{V}, t) = 0, 1_n^T \boldsymbol{T} \leq \eta \cos\theta, \} \tag{A4}$$

The set $\omega(\boldsymbol{x})$ is the intersection of a sphere, a hyperplane, and the half-space defined by another hyperplane. Thus, $\omega(\boldsymbol{x})$ itself is convex and bounded. For $\boldsymbol{p}_V \neq 0$, the Hamiltonian is a nonconstant convex (linear) function of $\boldsymbol{T}$. Hence, a maximizing $\boldsymbol{T}^*$ is guaranteed to exist on the boundary of $\omega(\boldsymbol{x})$ [24], and it satisfies the KKT conditions similar to Eq. (31) (plus a term $\lambda_3\gamma$ associated with $\gamma^T(\boldsymbol{r}, t)\boldsymbol{T} + \phi(\boldsymbol{r}, \boldsymbol{V}, t) = 0$ this time) and Eq. (32). The same arguments as used the proof of Lemma 1 will show that $\|\boldsymbol{T}^*\| = \eta$, and $\|\boldsymbol{T}^*\| = \eta^*$ when η takes its optimal value.

Appendix B: Proof of Lemma 3

Because the jump conditions such as those in Eqs. (40) and (41) generally involve $\boldsymbol{p}_V$, a finite interval where $\boldsymbol{p}_V = 0$ can only be in a subinterval separated by two adjacent jump conditions. First, assume that such an interval does not overlap with $[t_{\text{in}}, t_{\text{out}}]$ in which $h(\boldsymbol{r}, t) = 0$ [cf. Eq. (38)]. The same arguments as in the proof of Lemma 1 will show $\boldsymbol{p}_r = \boldsymbol{p}_V = 0$ in this interval, resulting in the condition for the Hamiltonian defined in Eq. (24):

$$H = -\left(\frac{p_m}{\boldsymbol{v}_{\text{ex}}} + p_0\right)\eta \tag{B1}$$

If $(p_m/\boldsymbol{v}_{\text{ex}} + p_0) > 0$, the optimality condition of Eq. (28) with respect to η in the set $\mathcal{U}_\eta$ defined as

$$\mathcal{U}_\eta = \{\eta | {}_n^T(t)\boldsymbol{T} \leq \eta \cos\theta, 0 \leq \eta \leq T_{\max}\} \tag{B2}$$

[§]Note that Theorem 22 in [23] applies to first-order state inequality constraint $g(\mathbf{x}) \leq 0$. But, in the notation of [23], what is fundamental in the proof is the first-order time derivative of the constraint $p(\boldsymbol{x}, \boldsymbol{u}) = \dot{g}(\boldsymbol{x})$. For a second-order constraint, the proof would remain essentially the same if $p(\boldsymbol{x}, \boldsymbol{u})$ is replaced by the second-order time derivative of the constraint $q(\boldsymbol{x}, \boldsymbol{u}, t)$, as in our case.

should take the lower bound of this set. As argued in the proof of Lemma 1, the lower bound of the set $\mathcal{U}_\eta$ is $\eta = 0$ under Assumption 1, thus $H = 0$; if $(p_m/v_{ex} + p_0) = 0$, we still have $H = 0$ regardless of what value $\eta^* \in [0, T_{max}]$ is. Because the system equations (12–14) are autonomous, the performance index [Eq. (15)] is not an explicit function of time, the problem has a fixed final time t_f, and the continuity of the Hamiltonian is not affected by the jump conditions of Eqs. (40) and (41), it follows that the optimal value of H is a constant throughout $[0, t_f]$ [23]. But both of the previous two possibilities imply that $H = 0$, irrespective of any value of t_f. Given that the $H(t_f)$ represents the influence of the variation of t_f on the performance index [25], such an invariance of the cost with respect to any t_f is not possible for the problem at hand. Therefore, the condition that $(p_m/v_{ex} + p_0) \geq 0$ can be ruled out, and the only remaining possibility is that $(p_m/v_{ex} + p_0) < 0$. From Eq. (27) it is clear that p_m is constant when $\boldsymbol{p}_V = 0$, and so is $(p_m/v_{ex} + p_0)$. The maximization of H in Eq. (B1) with respect to η over the set $\mathcal{U}_\eta$ in Eq. (B2) calls for the optimal η^* to take the upper bound of $\mathcal{U}_\eta$. But it is pointed out in the proof of Lemma 1 that $\mathcal{U}_\eta = \{\eta | 0 \leq \eta \leq T_{max}\}$ [cf. Eq. (36)]. Hence $\eta^* = T_{max}$.

If the constraint in Eq. (38) is not active anywhere or is active only at some isolated points ($t_{in} = t_{out}$), the previous discussion already covers the case. Next, consider the case when the interval $[t_{in}, t_{out}]$ has finite length ($t_{out} > t_{in}$), and the interval in which $\boldsymbol{p}_V = 0$ is contained in $[t_{in}, t_{out}]$. In the interval $[t_{in}, t_{out}]$, the costate equation for $\boldsymbol{p}_V$ becomes [23]

$$\dot{\boldsymbol{p}}_r = \frac{1}{\|\boldsymbol{r}\|^3}\boldsymbol{p}_V - \frac{(\boldsymbol{p}_V^T\boldsymbol{r})}{\|\boldsymbol{r}\|^5}\boldsymbol{r} + D(\boldsymbol{x}, \boldsymbol{T}, t)\boldsymbol{p}_r + E(\boldsymbol{x}, \boldsymbol{T}, t)\boldsymbol{p}_V \tag{B3}$$

$$\dot{\boldsymbol{p}}_V = -\boldsymbol{p}_r + F(\boldsymbol{x}, \boldsymbol{T}, t)\boldsymbol{p}_r + G(\boldsymbol{x}, \boldsymbol{T}, t)\boldsymbol{p}_V \tag{B4}$$

where D-G are 3×3 matrices from a dyad formed by $\partial q(\boldsymbol{x}, \boldsymbol{T}, t)/\partial \boldsymbol{x}$ and another time-dependent vector in R^6. See the proof of Theorem 22 in [23] for detail.¶ From Eq. (B4), when $\boldsymbol{p}_V = 0$ in any finite subinterval in $[t_{in}, t_{out}]$, $\boldsymbol{p}_r$ will have to vanish simultaneously in general, and consequently $\boldsymbol{p}_V = \boldsymbol{p}_r = 0$ throughout $[t_{in}, t_{out}]$ when combining Eqs. (B3) and (B4). Hence, the Hamiltonian reduces to Eq. (B1) again. The optimal η will be determined from condition (A2), which for η is over the same set $\mathcal{U}_\eta$ in Eq. (B2). Therefore, the same arguments employed in the preceding paragraph will again lead to $\eta^* = T_{max}$.

References

[1] Goodman, J. L., "History of Space Shuttle Rendezvous and Proximity Operations," *Journal of Spacecraft and Rockets*, Vol. 43, No. 5, 2006, pp. 944–959. doi:10.2514/1.19653

[2] Goodman, J. L., "History of Space Shuttle Rendezvous," NASA Johnson Space Center, Rept. JSC-63400, Houston, TX, Oct. 2011.

[3] Woffinden, D. C., and Geller, D. K., "Navigating the Road to Autonomous Orbital Rendezvous," *Journal of Spacecraft and Rockets*, Vol. 44, No. 4, 2007, pp. 898–909. doi:10.2514/1.30734

[4] Goodman, J. L., and Brazzel, J. P., "Rendezvous Integration Complexity of NASA Human Flight Vehicles," *32nd Annual AAS Guidance and Control Conference*, American Astronomical Society Paper 09-065, Washington, DC, Jan. 2009.

[5] D'Souza, C., Hanak, F. C., Spehar, P., Clark, F. D., and Jackson, M., "Orion Rendezvous, Proximity Operations, and Docking Design and Analysis," *AIAA Guidance, Navigation and Control Conference and Exhibit*, AIAA Paper 2007-6683, Aug. 2007.

[6] Goodman, J. L., "Challenges of Orion Rendezvous Development," *AIAA Guidance, Navigation and Control Conference and Exhibit*, AIAA Paper 2007-6682, Aug. 2007.

[7] Clohessy, W. H., and Wiltshire, R. S., "Terminal Guidance for Satellite Rendezvous," *Journal of the Aerospace Sciences*, Vol. 27, No. 9, 1960, pp. 653–674.

[8] Jezewski, D. J., Brazzel, J. P., Prust, E. E., Brown, B. G., Mulder, T. A., and Wissinger, D. B., "A Survey of Rendezvous Trajectory Planning," *AAS/AIAA Astrodynamics Conference*, American Astronomical Society Paper 91-505, Aug. 1991.

[9] Kachmar, P. M., and Chu, W., *Mars Initiative Rendezvous Analysis*, Charles Draper Lab., Cambridge, MA, May 1990.

[10] Carter, T. E., and Humi, M., "Fuel-Optimal Rendezvous Near a Point in General Keplerian Orbit," *Journal of Guidance, Control, and Dynamics*, Vol. 10, No. 6, 1987, pp. 567–573. doi:10.2514/3.20257

[11] Acikmese, B., and Ploen, S. R., "Convex Programming Approach to Powered Descent Guidance for Mars Landing," *Journal of Guidance, Control, and Dynamics*, Vol. 30, No. 5, 2007, pp. 1353–1366. doi:10.2514/1.27553

[12] Blackmore, L., Acikmese, B., and Scharf, D. P., "Minimum Landing Error Powered Descent Guidance for Mars Landing Using Convex Optimization," *Journal of Guidance, Control, and Dynamics*, Vol. 33, No. 4, 2010, pp. 1161–1171. doi:10.2514/1.47202

[13] Acikmese, B., Carson, J. M., and Blackmore, L., "Lossless Convexification of the Soft Landing Optimal Control Problem with Non-Convex Control Bound and Pointing Constraints," *IEEE Transactions on Control Systems Technology* (submitted for publication).

[14] Acikmese, B., and Blackmore, L., "Lossless Convexification for a Class of Optimal Problems with Nonconvex Control Constraints," *Automatica*, Vol. 47, No. 2, 2011, pp. 341–347. doi:10.1016/j.automatica.2010.10.037

[15] Alizadeh, F., and Goldfarb, D., "Second-Order Cone Programming," *Mathematical Programming*, Vol. 95, No. 1, 2003, pp. 3–51. doi:10.1007/s10107-002-0339-5

[16] Lobo, M. S., Vandenburghe, L., Boyd, S., and Lebret, H., "Applications of Second-Order Cone Programming," *Linear Algebra and Its Applications*, Vol. 284, 1998, pp. 193–228. doi:10.1016/S0024-3795(98)10032-0

[17] Boyd, S., and Vandenberghe, L., *Convex Optimization*, Cambridge Univ. Press, Cambridge, England, U.K., 2004, Chaps. 2–5, 9–11.

[18] Nesterov, Y., and Nemirovsky, A., *Interior-Point Polynomial Algorithms in Convex Programming*, Society for Industrial and Applied Mathematics, Philadelphia, PA, 1994, Chaps. 2–6.

[19] Wright, S. J., *Primal-Dual Interior-Point Methods*, Society for Industrial and Applied Mathematics, Philadelphia, PA, 1997, Chaps. 1–11.

[20] Andersen, E. D., Roos, C., and Terlaky, T., "On Implementing a Primal-Dual Interior-Point Method for Conic Quadratic Optimization," *Mathematical Programming*, Vol. 95, No. 2, 2003, pp. 249–277. doi:10.1007/s10107-002-0349-3

[21] Wang, Y., and Boyd, S., "Fast Model Predictive Control Using Online Optimization," *IEEE Transactions on Control Systems Technology*, Vol. 18, No. 2, 2010, pp. 267–278. doi:10.1109/TCST.2009.2017934

[22] Mattingley, J., and Boyd, S., "Real-Time Convex Optimization in Signal Processing," *IEEE Signal Processing Magazine*, Vol. 27, No. 3, May 2010, pp. 50–61.

[23] Pontryagin, L. S., Boltyanskii, V. G., Gramkreledze, Q. V., and Mishchenko, E. F., *The Mathematical Theory of Optimal Processes*, Wiley-Interscience, New York, 1962, Chaps. 1, 2, 6.

[24] Berkovitz, L. D., *Convexity and Optimization in R^n*, Wiley, New York, 2002, Chap. 4.

[25] Bryson, A. E., and Ho, Y. C., *Applied Optimal Control*, Hemisphere, Washington, DC, 1975, Chap. 3.

[26] Jezewski, D. J., "An Optimal, Analytic Solution to the Linear-Gravity, Constant-Thrust Trajectory Problem," *Journal of Spacecraft and Rockets*, Vol. 8, No. 7, 1971, pp. 793–796. doi:10.2514/3.30320

[27] Carson, J. M., and Acikmese, B., "A Model Predictive Control Technique with Guaranteed Resolvability and Required Thruster Silent Times for Small-Body Proximity Operations," *AIAA Guidance, Navigation and Control Conference and Exhibit*, AIAA Paper 2006-6780, Aug. 2006.

[28] Lu, P., Griffin, B., Dukeman, G., and Chavez, F., "Rapid Optimal Multi-Burn Ascent Planning and Guidance," *Journal of Guidance, Control, and Dynamics*, Vol. 31, No. 6, 2008, pp. 1656–1664. doi:10.2514/1.36084

[29] Banks, S. P., and Dinesh, K., "Approximate Optimal Control and Stability of Nonlinear Finite- and Infinite-Dimensional Systems," *Annals of Operations Research*, Vol. 98, 2000, pp. 19–44. doi:10.1023/A:1019279617898

¶The footnote in the proof of Lemma 2 applies here as well.

[30] Ström, T., "On Logarithmic Norms," *SIAM Journal of Numerical Analysis*, Vol. 12, No. 5, 1975, pp. 741–753.
[31] Hofer, E., and Tibken, B., "An Iterative Method for the Finite-Time Bilinear Quadratic Control Problem," *Journal of Optimization Theory and Applications*, Vol. 57, No. 3, 1988, pp. 411–427. doi:10.1007/BF02346161
[32] Aganovic, Z., and Gajic, Z., "The Successive Approximation Procedure for Finite-Time Optimal Control of Bilinear Systems," *IEEE Transactions on Automatic Control*, Vol. 39, No. 9, 1994, pp. 1932–1935. doi:10.1109/9.317128
[33] Lee, E. B., and Markus, L., *Foundations of Optimal Control Theory*, Wiley, New York, 1967, pp. 239–307, Chap. 4.
[34] Chobotov, V. A., *Orbital Mechanics*, 3rd ed., AIAA, Reston, VA, 2002, pp. 193–208, Chap. 9.
[35] Tang, G., "Suboptimal Control for Nonlinear Systems: A Successive Approximation Approach," *Systems and Control Letters*, Vol. 54, 2005, pp. 429–434. doi:10.1016/j.sysconle.2004.09.012
[36] Stoer, J., and Bulirsch, R., *Introduction to Numerical Analysis*, Springer–Verlag, New York, 1980, pp. 117–121, Chap. 3.